ENGINEERING LEDS: DESIGNING A REMOTE PHOSPHOR CONFIGURATION FOR HIGH LUMINANCE APPLICATIONS

by

Michael Maxim Schur

A Thesis Submitted to the Faculty of the

JAMES C. WYANT COLLEGE OF OPTICAL SCIENCE

In Partial Fulfilment of the Requirements

For the Degree of

MASTER OF SCIENCE

In the Graduate College

THE UNIVERSITY OF ARIZONA

2024

THE UNIVERSITY OF ARIZONA
GRADUATE COLLEGE

As members of the Master's Committee, we certify that we have read the thesis prepared by **Michael Maxcim Schur,** titled ***Engineering LEDs: Designing a Remote Phosphor Configuration for Laser Driven High Luminance Sources - An Analysis through Simulation*** and recommend that it be accepted as fulfilling the thesis requirement for the Master's Degree.

Professor R. John Koshel Date: 5/2/2024

Professor Florian Willomitzer Date: 5/3/2024

Luis Sagastume (May 3, 2024 20:57 EDT) Date: 05/03/2024

Luis Sagastume

Final approval and acceptance of this thesis is contingent upon the candidate's submission of the final copies of the thesis to the Graduate College.

I hereby certify that I have read this thesis prepared under my direction and recommend that it be accepted as fulfilling the Master's requirement.

Professor R. John Koshel Date: 5/2/2004
Master's Thesis Committee Chair
Wyant College of Optical Sciences

ACKNOWLEDGEMENTS

I would like to first thank my advisor and committee chair, Professor Koshel, for going beyond the role of an advisor for a thesis defense, but rather being a mentor who consistently provided invaluable guidance and support throughout this journey.

Additionally, I extend my gratitude to the two committee members Prof. Willomitzer and industry committee member Luis Sagastume, whose mentorship and leadership, particularly during my tenure at Rivian, influenced this thesis.

Thank you to my family and friends whose continuous support has provided me with the energy and determination to successfully navigate the challenges of completing the master's program.

"And you, Ring-bearer,' she said, turning to Frodo. 'I come to you last who are not last in my thoughts. For you I have prepared this.' She held up a small crystal phial: it glittered as she moved it, and rays of white light sprang from her hand. 'In this phial,' she said, 'is caught the light of Eärendil's star, set amid the waters of my fountain. It will shine still brighter when night is about you. May it be a light to you in dark places, when all other lights go out."

— *The Fellowship of the Ring*, "Farewell to Lórien"

TABLE OF CONTENTS

ABSTRACT

Laser-driven white light sources promise super high brightness, luminous flux and high directionality for solid-state lighting applications. In this thesis we use the standard Cassegrain model, but in reverse, to develop a novel LED device package that directs, and mixes all lights of the system. Utilizing LightTools® as our primary simulation software, we identified and optimized important variables inside a micro-LED configuration to show that the model device package can emit up to 360 lumens per watt all while keeping fidelity to D65 CCT and CIE color values. Next, we generated a rayfile to export results for evaluation as a light source using LucidShape. Subsequently, we analyzed the rayfile data integrated into an ADB projection system, enabling detailed assessment of the LED's optical performance in comparison to an industry standard ADB light source. We demonstrate that the prototype LED outperforms commercial LEDs in terms of luminous efficacy and projection efficiency. These findings not only show great promise for advancing solid-state lighting technology but also open up new avenues for design to address decreasing energy consumption in commercial lighting applications.

LIST OF FIGURES

I. Introduction

A. Motivation

In 2010, leading car manufacturers including Mercedes-Benz, Audi, and Opel, presented adaptive driving beam (ADB) to the United Nations Economic Commission for Europe's Working Party on Lighting and Light Signaling (GRE) in Geneva (Barry, 2022). ADB, is an innovative headlamp design which aims to enhance nighttime driving safety by uniformly illuminating essential areas for the driver while deflecting beam patterns away from oncoming motorists. Shortly after this meeting, ADB was swiftly adopted and integrated into the Economic Commission of Europe (ECE) regulations. In response to ADB's success in Europe, Toyota initiated lobbying efforts in 2013 with the U.S. government, petitioning the National Highway Traffic Safety Administration (NHTSA) to approve ADB systems for the U.S. market (Kaplan, 2023). By 2018, NHTSA officially announced its consideration for approving the technology. However, the momentum stalled as no new regulations were implemented to allow ADB for sale in the U.S.

The Infrastructure Bill that passed in 2022 compelled lawmakers to establish regulations concerning ADB and on February 15th, 2022, NHTSA announced that they, “issued a final rule allowing automakers to install ADB headlights to new vehicles (NHTSA, 2022).” With approval finally completed, numerous headlight technology advancements including laser driven (LD) light sources are anticipated to enter the U.S. market to supply the increase in luminous demand. The prolonged lobbying to permit ADB has led to significant investment in optical research and development within the automotive industry, OEMs seek to integrate traditional lamps with complex illumination, imaging, and sensor systems.

The aim of this thesis project is to develop a LD LED module for potential automotive use, specifically as a source for exterior signal functions such as daytime running lamps (DRL), high beams (HB), or low beams (LB). Two optical systems are to be developed: the first is to produce a laser-to-phosphor (LtP) LED packaging, and the second is to integrate the LtP-LED in an exterior lighting system for performance analysis. Additionally, given the compact size of these potential light sources, this thesis will discuss other possible applications, particularly in micro-display technology and others that require high-intensity and small-packaging.

B. Light Emitting Diodes (LED)

Due to an increased emphasis on energy efficiency, LED researchers are actively searching for methods to increase generation of white light per unit watt. This is important for electric vehicles looking to reduce their energy budget, as a result active studies are pointing towards utilizing lasers for headlamps as they are much brighter and cost about two-thirds the amount of energy when comparing to traditional sources (Ulrich, 2013).

A traditional LED as shown in the schematic of Figure 1, has a phosphor layer overlaying a GaN alloy wherein the alloy generates blue light through electroluminescence. When a current is applied to the semiconductor GaN alloy a recombination of free holes and electrons occur, free electrons move from the n-type region to the p-type region vice versa. The area in which the recombination of the free holes and electrons occur is called the active

region (i.e., depletion region), and is where photon are emitted. The location at which the n-

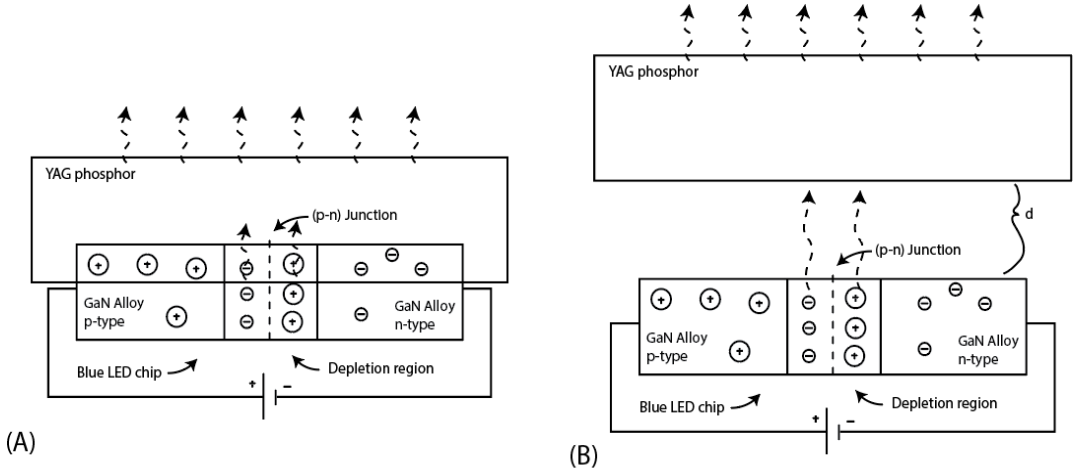

Figure 1. Schematic of two LED configurations (A) traditional LED the active layer (i.e., GAN alloy) sits underneath a phosphor layer and the layers touch. (B) for remote LEDs the active layer and phosphor layer are separated by a distance 'd' (Schur Michael M., 2024).

type material and the p-type material meet is considered the p-n junction[1], this is where the term junction temperature derives its name. A remote phosphor simply implies that the phosphor layer is a distance 'd' away from the active layer of the LED. One immediate benefit for having a remote phosphor is that the phosphor layer absorbs less heat generated by the p-n junction and therefore can convert more of the excitation radiation without additional thermal oversaturation from the active region. In traditional LEDs the active layer generates blue light in a Lambertian curve, for most remote applications a laser diode replaces a Lambertian emitter, and the excitation beam is assumed to be a concentrated gaussian.

[1] The p-n junction is where most thermal calculations for LED derives, as it is the central point where heat is generated.

C. Monte Carlo simulation methods

For this study we chose Synopsy®'s LightTools®[2] which is used for designing, optimizing, and analyzing solutions for illumination optics. LightTools® performs non-sequential[3] Monte Carlo ray tracing with their illumination module and have many core features that we take advantage of for this project, mainly their optimization module, and advanced physics module, the advanced physics module including phosphor particle modeling. Specifically for our simulations we use forward ray tracing which simulates radiant flux propagation across the model (LightTools, 2024). In forward ray tracing, rays are traced from random points within the source's volume or on its surface, shooting off in random angles based on probabilistic functions, using Monte Carlo calculations, that represent the emissive behavior of light sources. The rays hold information on wavelength and a set power (from 1 to 0) which attenuates as it passes through materials set in the simulation model. Once the ray passes through the medium it will now have a power reduced by the absorptive coefficient at the respective wavelength.

When the Monte Carlo method is applied to a phosphor it takes into consideration emission, absorption, excitation, and scattering. Each incident ray to the phosphor surface has a specific amount of power attenuated by its wavelength, the power is modified when hitting the phosphor particle, as it is either absorbed, absorbed and used for emission, or scattered. When the ray enters the phosphor material LTs calculates the average distance that a ray travels throughout the material before it is likely to interact with a phosphor particle, determined by mean free path (MFP),

[2] LightTools(64) 2023.03 Build: 2023.02.03.1516.40868584 was used.

[3] Non-sequential ray tracing, typically used in illumination modeling and/or stay-light analysis, allows a ray to intersect surfaces in your model multiple times and can intersect those surfaces in any order.

$$l = \frac{1}{n(\sigma_{scat} + \sigma_{abs})}$$

where l is the mean free path, n is the density of particles, σ_{scat} is the scattering cross-sectional area, and σ_{abs} is absorption cross-sectional area (Zollers, 2011). Stochastic Monte Carlo calculations are done to determine the emission distribution from the excited phosphor particle (Koshel, 2013)[4].

II. Simulation

In Chapter II, we explore three distinct simulation models to study and develop an LED. In the first study, *Simulation I: L-Phosphor,* we simulate a simple laser-to-phosphor model to identify critical variables influencing light generation and propagation. In the second study, *Simulation II: Inverse-Cassegrain* ("IC"), we apply the lessons learned in A to create an LED configuration using an IC optical structure and optimize the geometry with phosphor variables for desired lumen output, color, and emission curve. In the third study, *Simulation III: LucidShape ADB system,* we import results from LightTools® and insert them into LucidShape as a light source to use inside of an ADB projector system. Lastly, we will compare the results of our system to an industry standard ADB chip.

A. Simulation I: L-Phosphor

The focus of *Simulation I* is to investigate several physical parameters of a phosphor when excited by a high-intensity beam (i.e., LD). First, we identify important variables inside Synopsys®'s LightTools® while also postulating those beyond the capability of

[4] Essentially all modified variables in a phosphor matrix will either cause an increase or decrease in mean free path of the ray inside of the phosphor matrix. This will later determine how much conversion, luminous output and color will be generated by the system.

simulation, subsequently discussing their potential effects on results. We attempt to balance a wholistic understanding since it is, in part, a feasibility study. However, it is limited in scope to simulation and not validated through laboratory experimentation but via meta-analysis of reported information. Primary variables were grouped into three categories: light source, phosphor, or matrix (i.e., phosphor encapsulant), as listed in Table 1.

Table 1. Listed outline of identified controllable parameters in LightTools®, there are many other controllable variables for this experiment however this list comprises a theorized collection of most important variables that influences, lumen generation and color.

Light Source	**Phosphor**	**Encapsulant/Matrix**
Flux/Power	Thickness	
Angular Distribution	Height & Width	
Spatial Distribution	Geometric Volume	
Central Wavelength	*Excitation Spectrum*	*Absorption Spectrum or Transmission Spectrum*
Spectral Region	*Emission Spectrum*	
Type	*Absorption Spectrum*	
	Volume%	Volume %
	Particle Density	Particle Density
	Refractive Index	Refractive Index
	Mie Particle Size	Mie Particle Size

The setup for simulation I is illustrated in Figure 2**.** In this figure the blue light source is set to a distance from the origin represented by ‘a’. The phosphor which is a distance ‘b’ away from the origin comprises of a thickness ‘t’, lastly ‘d’ denotes the total distance between the light source and the phosphor along the z-axis.

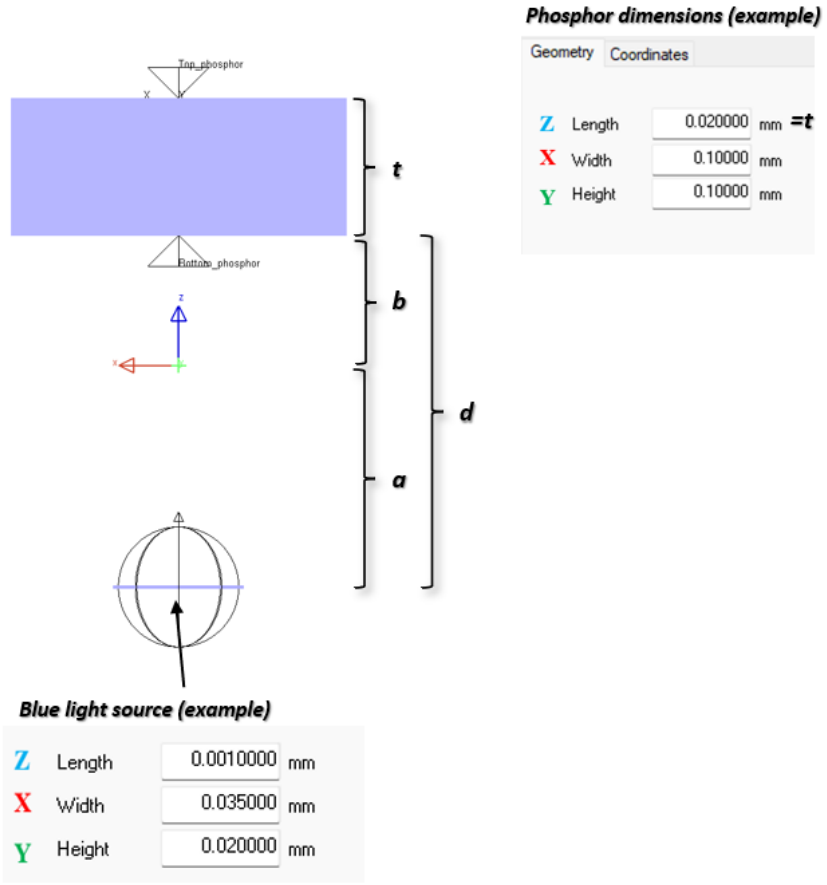

Figure 2. Simulation I setup, within LightTools. A high intensity beam to a phosphor cube. The cube comprising of thickness 't' (Schur Michael M.).

In the context of configuring an LED for an exterior automotive lighting, our investigation first focuses on utilizing Yttrium Aluminum Garnet doped with Ce^{3+} “YAG:Ce” ($Y_3Al_5O_{12}:Ce^{3+}$). This inorganic phosphor is a popular choice for white light generation due to its high efficiency, cost-effectiveness, ease of fabrication, and precise

control over chromaticity (Shuyang Bao, 2022). Additionally, for simulating without direct testing in the lab it is considered best practice to first choose materials which are well documented, which YAG phosphor are. YAG:Ce phosphors absorb wavelengths of blue photon energy (i.e., excitation wavelength) that are then down-converted[5] and re-emitted by

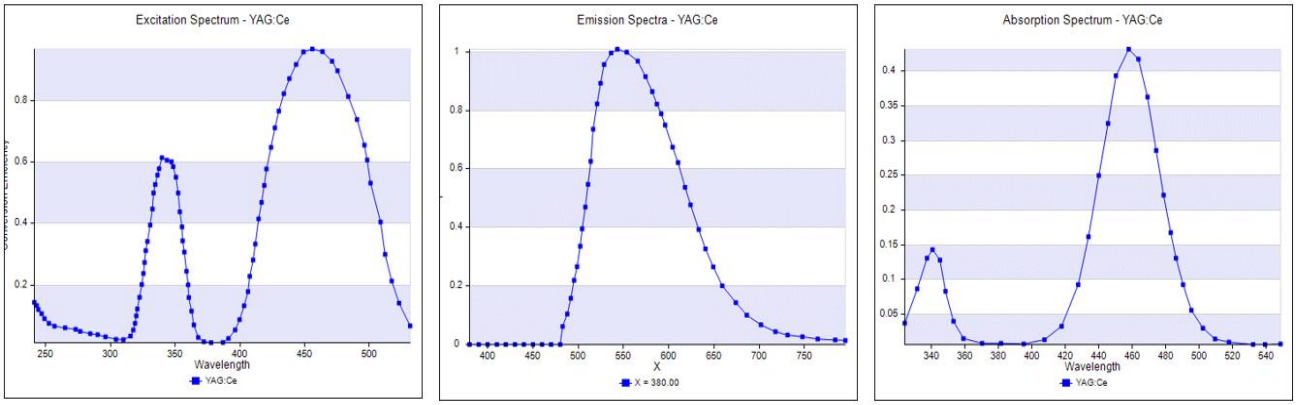

Figure 3. YAG:Ce3^{+} phosphor's absorbance spectra, excitation spectra and emission spectra. Extracted from (Anne C. Berends, 2020) digitized by Schur Michael M..

the phosphor isotopically. The phosphor particles then generate yellow light in the 500-750 nm wavelength range (i.e., emission wavelengths), typically peaking at 554 nm at room temperature (Anne C. Berends, 2020). Figure 3 shows the absorbance, emission and excitation spectra which were digitized using LightTools® and used for simulation.

In respect to the crystalline structure of a YAG:Ce particles (CRYTUR, 2024), when a photon interacts with a phosphor particle, several events may occur. The particle depending on size and composition, in simulation, can either: absorb, refract/transmit, reflect/scatter, and/or absorb and emit light, all of which are wavelength-dependent calculations[6] (Field

[5] Down conversion is in reference to a high energy photon (e.g., blue or ultraviolet wavelengths) being converted into lower-energy (i.e., longer-wavelengths). Energy here is defined in terms of Plank's energy equation, wherein E is proportional to 1/λ.

[6] Diffraction was omitted from the discussion as our simulation in LightTools primarily models light propagation as rays rather than waves, neglecting wave phenomena such as polarization and phase.

Guide to Atmospheric Optics, 2019). *See* Figure 4. Absorption is understood as fundamentally a quantum process where an atom absorbs energy from incident photons, luminescence occurs when an electron from the atom is 'promoted' from ground state to an

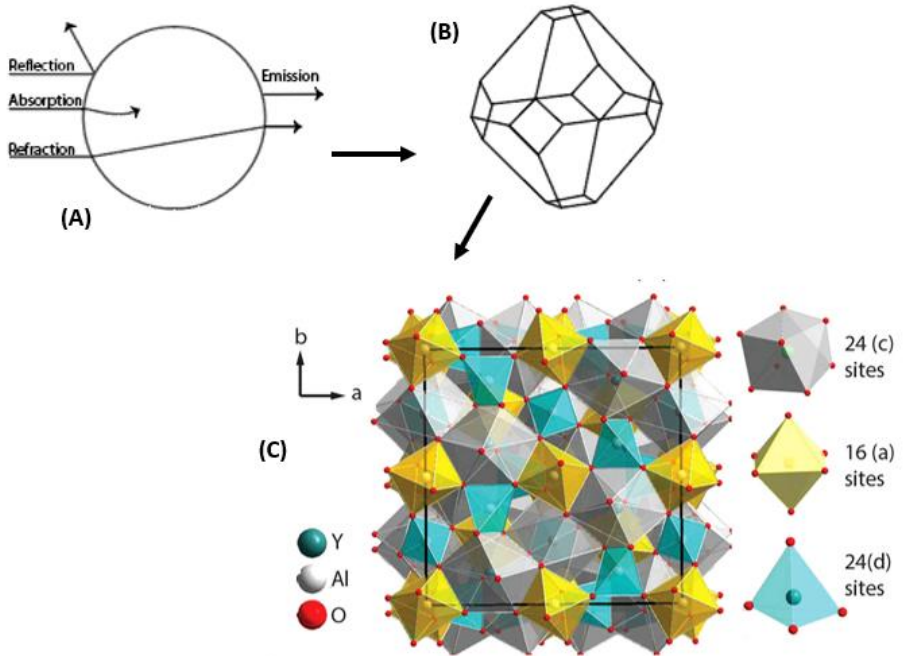

Figure 4. (A) is an illustration of a simple phosphor particle and listing what may occur within simulation. (B) a more realistic image of what particle structure may look like. (C) Crystaline composition of YAG particles. A and B drawn by Michael Schur. C taken from (Anne C. Berends, 2020).

excited state. The excited state then decays to a meta-stable state (i.e., Stokes loss-- heat) before hitting the ground state emitting a longer wavelength photon. This is understood by the collected spectra of emission, excitation and absorption, there is an option in LT to use quantum yield replacing excitation spectra. Recall earlier that the MFP is used to calculate the probability that a ray will travel inside a phosphor medium without hitting a phosphor particle. Using MFP probability if a ray is determined to hit a phosphor particle and has the

Consequently, our focus remains on scattering, which aligns with the ray-tracing approach employed in our simulations to study the optical behavior of phosphor particles. Wherein each ray is a metric of intensity, 0 to 1.

proper absorption wavelength LT then calculates if the incident wavelength causes an electron to jump the bandgap and therefore stimulates emission. For the simulation studies we use excitation spectrum instead of internal quantum yield calculations because most literature that includes emission spectra also include a correlating absorption spectrum and therefore includes Stoke's shift (i.e., the difference of absorption and emission spectra max wavelengths).

Another assumption is that the particles undergo Mie scattering. Rays that encounter a phosphor particle have a probabilistic designation of either being absorbed or scattered and due to the size of the particle subjected to the wavelength of light Mie Theory is employed. Though there are a few single-scattering theories for this thesis we focus on Mie scattering[7].

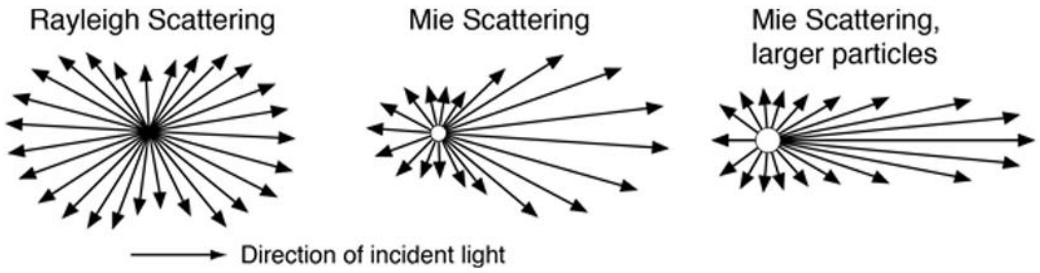

Figure 5. Different scattering models which are chosen based on particle size and wavelength of incident light (Hahn, 2009).

There are a few scattering theories to consider, Rayleigh, Mie and geometric. The general rule of understanding when to apply one over the other is expressed in the formula below, which assumes dielectric microspheres suspended in water. The formula shows that,

$$\alpha = \frac{2\pi r}{\lambda}$$

[7] The single-scattering theories discussed herein are based on the assumption of spherical-shaped, non-interacting particles.

Where r is the radius of the sphere (particle) and λ is the wavelength of the incident light. When $2\pi r \ll \lambda$ ($\alpha \ll 1$), the situation is described by the Rayleigh formula. Mie scattering is described when $2\pi r \approx \lambda$ ($\alpha \approx 1$), lastly when $2\pi r \gg \lambda$ ($\alpha \gg 1$) we have what's called Mie scattering of larger particles or geometric scattering (Hahn, 2009). In this simulation the excitation beam is 445-450 nm and the particle size of a YAG phosphor can range from 1 nm[8] to 1500 nm, based on wavelength and radius of particles we can assume Mie scattering throughout the system or geometric scattering if particle size of 1000 nm or larger are used.

Inside the phosphor matrix it is assumed that the phosphor particles will act as volume scatters, meaning that statistically these particles will geometrically change the direction of any incident wavelengths based on their respective refractive index and sizes as explained above. LT allows us to define the volume scattering models as: phosphor, Mie, Henyey-Greenstein, Gegenbauer, User-Defined and User-Defined DLL. By selecting 'phosphor' we simulate particles that convert light, additionally we use Mie Theory[9] to calculate the phosphor mean free path and the intensity distribution of unconverted rays. Later we also look at adding inert matrix scatters, these will be generated using Mie.

Using the Mie scattering model in LT we can specify density of particles (mm^{-3}), mean free path, transmissivity, and angular scattering distributions calculated based on Mie theory. In LT we set controls for a phosphor mean free path based on Mie Theory and the intensity distribution of unconverted rays set to isotropic, meaning that the scattered rays

[8] During the simulation process it was found that particle sizes of below 10 nm were given as a result of optimization, these effectively act as quantum dots. Further research for properly modeling quantum dot phosphor layers can be a branch of research stemming from this project as outlined in (Lee, 2023).

[9] The equations that relate the angular distribution of scattered light to these parameters were first derived by Gustav Mie in 1908 by solving Maxwell's equations at the boundary of a spherical particle. Only spherical particles are considered in the LightTools model.

will equally likely exit the particle at any given angle (Rayleigh Scattering, Mie Scattering, 2015)[10].

The computational aspect for Mie scattering can be complex and intensive, LT explains in their User Guide that many of the calculations are performed in LT prior to ray tracing to improve ray speeds. “For instance, the angular intensity distribution for a Mie scatterer is precomputed and stored in memory. These computations are performed whenever a Mie scatterer is first defined, or whenever a new spectral region is defined for a system with a Mie scatterer. The computations can take longer for continuous spectral regions than for discrete ones and may take a significant amount of time; for this reason, LightTools® displays a warning message while performing them.” Using volumetric scattering in most optical simulation models will exponentially increase not only simulation time but depending on RAM, may also be very difficult to use in the UI of the software, so it is important to realize these limitations and plan your simulation accordingly. This is mainly why we break every part down into simpler simulation studies and models.

Concerning particle size distribution, LightTools® allows us to control the distribution of particle sizes throughout the phosphor matrix. However, it is highly advised to limit the number of particle size entries to below 10 (e.g., 10 nm 50 nm and 90 nm, are three size

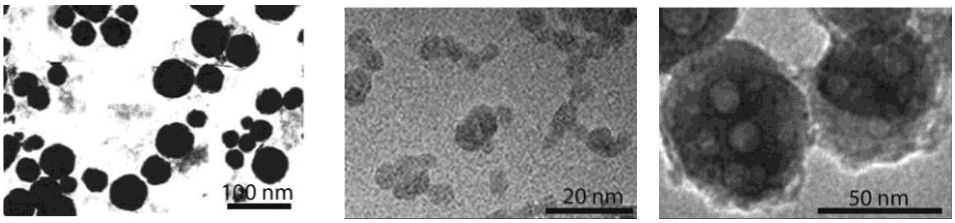

Figure 6. Transmissions electron microscopy and scanning electron microscopy images of nano YAG particles of various sizes ranging from 50nm-100nm. Extracted from, YAG:Ce3+ Phosphor: From Micron-Sized Workhorse for General Lighting to a Bright Future on the Nanoscale by Berends et., al.

[10] In LT Mie scattering does not track polarizing effects, all scattered rays are unpolarized—which is also why we chose to not study polarizing effects in this thesis.

entries) adding more can drastically increase simulation preparation time. Figure 6 show images under transmission electron microscopy of YAG nanoparticles, the synthesis of which was done via solvothermal route explained further in (Anne C. Berends, 2020). The important take away here when applying these images to LightTools® are; for one, we assume that the radius of the Mie Particles is constant and that the shape is perfectly spherical, Berends et., al. show particles may be formed so that they are well-defined spherical structures therefore this is a validated assumption. However, there is a plurality of different YAG particle synthesizing methods which result in larger clumped shapes. We can potentially increase accuracy of the simulation by defining a variant of Mie Particle sizes by using a gaussian size distribution (Yiman Wang, Modeling on phosphor sedimentation phenomenon during curing process of high power LED packaging, 2014) macro (since most size distributions follow this pattern), expressed in the equation below.

$$size(x) = e^{-\frac{(x-\mu)^2}{2\sigma^2}}$$

Where x is the radius of the Mie Particle (in nm), μ represents the average statistical size and, σ is a small standard deviation of the set of particle sizes. The limit of the optimization merit functions (discussed later) must consider the limit that these particles can be synthesized (as low as 5 nm) and is used as a starting limit for first optimizations, however, is not used as the ultimate limit in final optimization as there may be advances in technology to further enable smaller particle size. For this thesis we continue with a constant particle size, due to hardware constraints.

Concerning excitation beam sources:

Going back to the simulation set-up, a consideration on the type, shape, and emission of excitation beam needs to be discussed. We look toward semiconductor manufacturing to choose a feasible laser system. Recall that there are two types of LEDs, edge emitting and surface emitting. As shown in Figure 7, depending on which is chosen will depend on the shape of our propagation beam, for symmetry purposes we chose Vertical Cavity Surface-Emitting Laser (VCSEL), however either may ultimately be used for the function of our

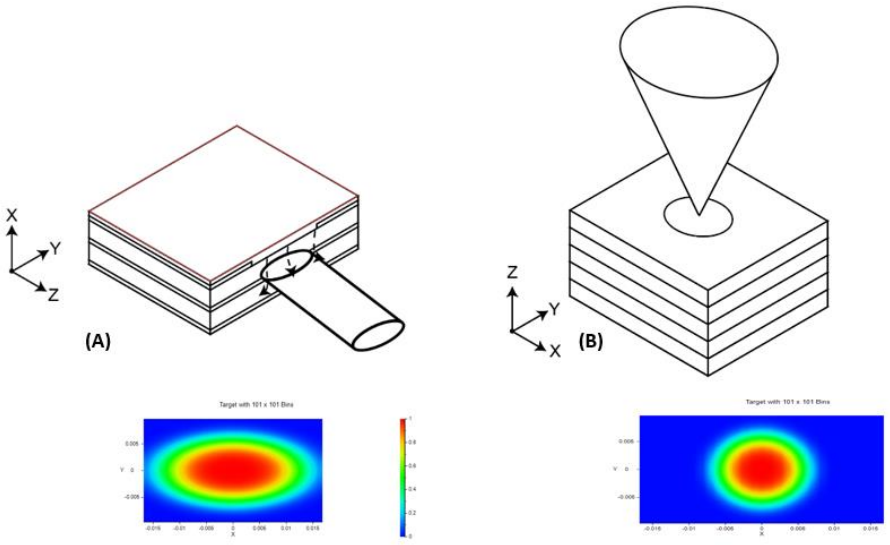

Figure 7 illustrates the optical characteristics of two distinct light-emitting devices. In panel (A), an isometric view of an edge-emitting LED (ELED) is depicted, accompanied by its corresponding spatial Gaussian profile. In this configuration, power emanates from the strip region towards the base of the ELED, leading to light emission from the active layer in the form of an oval beam profile. Conversely, panel (B) showcases a Vertical Cavity Surface-Emitting Laser (VCSEL), along with its associated spatial Gaussian beam profile, which exhibits a circular shape (ideal due to its symmetry) (Schur Michael M., 2024).

LED configuration. A more complete list comprises of potential laser sources are: Micro-LEDs (µLEDs), Edge-emitting lasers (EEL or ELED), Vertical cavity surface-emitting lasers (VCSELs), and Photonic Crystal Surface-emitting Lasers (PCSELs) (Kei Emoto, 2022) (Eiji Miyai, 2008).

ELEDs and VCSELs generate a beam pattern that is either circular or elliptical respectively, indium gallium nitride (InGaN) is the LED III-V semiconductor materials which is primarily responsible for delivering blue color (Mertens, 2024) in these systems. The spectral binning of these materials can range in wavelengths of ~360-800 nm (Kouno, 2016) however in the applications listed above the binning can range from ~0.05 nm-1.0 nm (Kei Emoto, 2022) with peak wavelengths at 450 or 431 nm (Yuanbin Gao, 2023). Gallium(III) nitride can generate wavelength of 380nm-417nm or indium gallium nitride at 450nm (Justin C.Johnson, 2002).

The radiant power for the light sources was set to 1.00 Watt. This was done for simplicity, but note the results are typically reported in lumens therefore each lumen reported is a theoretical lumen/watt luminous efficacy (LE) result for the system. It is important to keep in mind that radiant power greatly impacts conversion via thermal and optical saturation (later discussed), we ignore thermal properties because LT, outside of spectral data manipulation does not have a means to calculate these effects. The spectral data we extracted are from lab test results, which are done under thermal constraints. However when we change the sizes of not only the phosphor but the beam while keeping power constant we run into concerns that the simulated power will over saturate the system. Understanding this we keep the power at 1W, as it is easier to determine LE, knowing that we would need to ultimately scale source power back linearly normalizing results to the scaled power.

Beam modeling was done following the steps in “Laser Diode Sources” a pdf on Synopsys®’ portal (LightTools, 2024)[11]. Lasers have different divergence angles for x/y

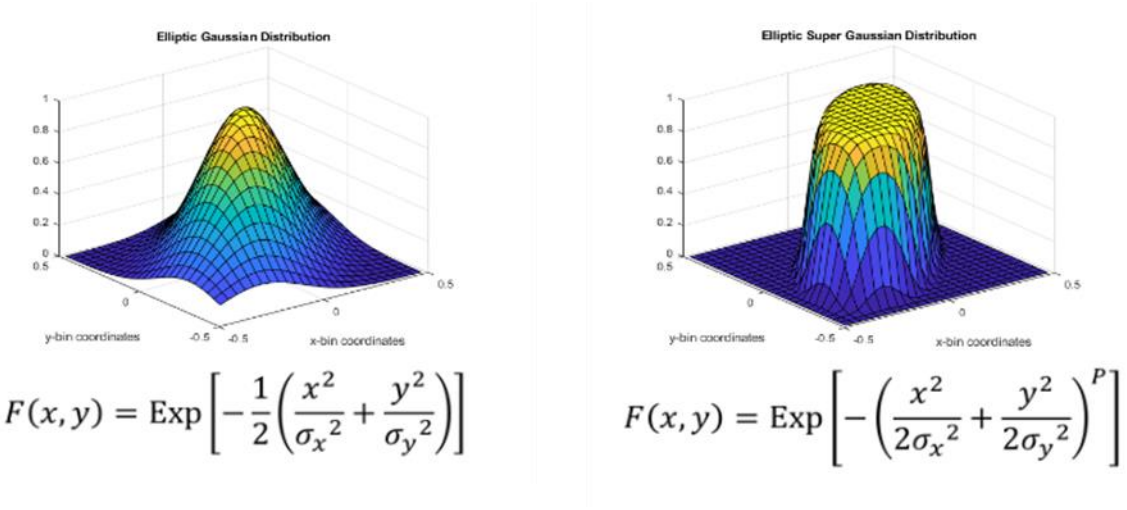

Figure 8. 3-dimensional view of an elliptic gaussian (left) and an elliptic super gaussian (right) distribution with their respective expressions. Super gaussians have a curve with a flatter top and a steeper drop at the sides, causing a uniform intensity distribution along a 2D surface cut overlay, for the non-super expression P=1 (LightTools Handbook).

axis, assuming projection in the z-dir, so it is common to assume that the light source may comprise a cross-section of an ellipse though are not limited to an ellipse as VCSELs propagate equally in both x/y positions. Figure 8 shows the difference in LT calculations for beam patterns, taken from the user module guide for visualization of the system’s excitation beam propagation calculations, used in these simulations. The spatial gaussian values σ_x σ_y (mm) are user input values and are ultimately constrained by the size, and distance the excitation beam is from the phosphor[12].

[11] Laser light sources in LightTools (LT) can be modeled in several ways: as a point source, a surface source, or a cuboid source. After evaluating each of these profiles, we chose the cuboid source because there are more controllable parameters in beam profiling.

[12] LT allows you to control the beam using a variety of gaussian profiles, among them are; spatial elliptic gaussian, spatial elliptic super gaussian, spatial rectangular super gaussian, angular gaussian, angular elliptic super gaussian, angular rectangular super gaussian. Because we are modeling a VCEL we continued with using spatial and angular super gaussian profiles.

Though LightTools® can simulate coherent ray tracing, polarization and phase of the rays comprising the lasers beam profile, we chose to omit adding these for a few reasons. For one this is beyond the scope of this thesis, the effects of polarization and phase on a phosphor matrix can be a research project on its own. Secondly, because the coherence properties of the excitation beam are assumed to be negligible when exciting a phosphor particle for emission, therefore we assume an incoherent source. Coherent source rays carry added data which compound when we need to simulate using hundreds of millions of rays.

Due to the natural divergence of lasers, some LtP systems discuss using an aspheric lens in front of the light source. In these systems the distance between the laser and phosphor is great enough so that the divergence angle creates a cross-sectional of the laser surface area subtending to the phosphor surface greater than the phosphor surface area and thus needs correction. Adding aspheric lenses, especially for micro systems is costly, additionally for micro system focal lengths the natural divergence angle of the laser can be used to determine the limited distance from the phosphor needs to be to the excitation beam, therefore an additional lens is not needed. Some examples of beam divergence angles are between 5-20 degrees in the slow axis and 10 to 40 degrees in the fast axis, for VCEL's it can be between from 1-5 degrees in both fast and slow axes. PCSELs (photo-crystal lasers) as discussed in "Wide-bandgap GaN-based watt-class photonic-crystal lasers" Emoto et., al. can be used to excite a phosphor matrix, and they have a less than 0.2-degree divergence angle along with a 0.05 nm band length. Ergo, there are many ranges of values to use for divergence and beam sizes.

With all that has been discussed in mind, we begin to simulate in a 360-degree detector, the basic LtP system. The goal is to observe how light in the system is generated and

propagates to lay the foundation for the next simulation which will look at developing optical geometry. In the initial results we immediately observe (in Figure 9) that the side of the phosphor the laser subtends has vastly greater luminous intensity than the opposite surface, that is because light that hits the first surface not only converts a portion of

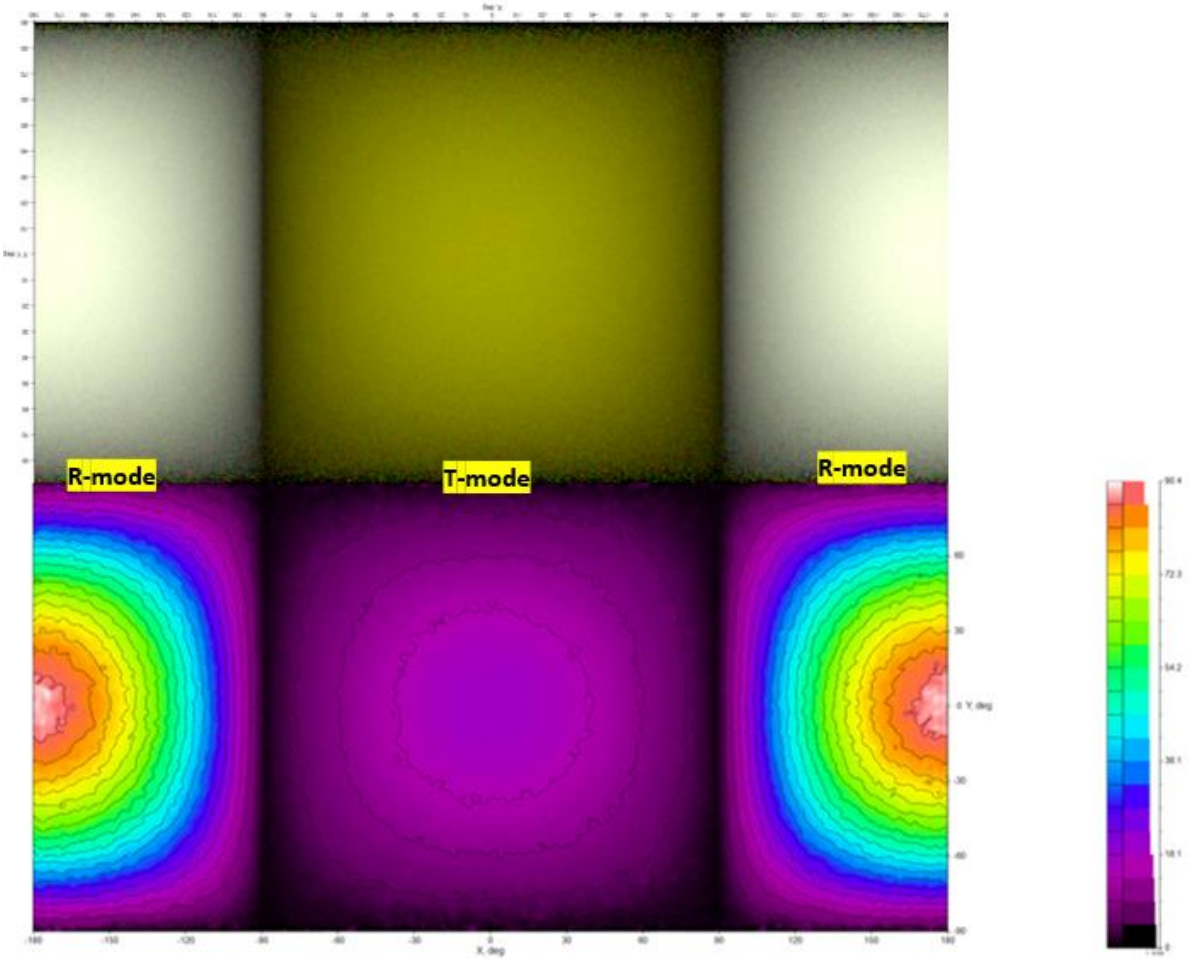

Figure 9. Real-color (top) and false-color intensity (bottom) distribution of the YAG phosphor in a spherical detector (IES type-A). Results are identified as being R-mode or T-mode (Schur Michael M., 2024).

phosphor particles but reflects the unconverted excitation beam[13]. We term the results of these two sides R-mode and T-mode. R-mode describes the surface where the excitation

[13] This is still true whether the surface has specular reflection or Lambertian reflection.

beam is reflected, and T-mode describes the side that transmits the remaining light (converted and unconverted) that propagates and exits the other end of the phosphor surface. A schematic representation of R and T mode can be seen in Figure 10. The phosphor was assumed to be suspended in silicone (DOW, 2024). The surface values were assumed to be 2% reflective and 98% transmissive, meaning that the reflection of the excitation beam was occurring due to the phosphor particles suspended inside the matrix.

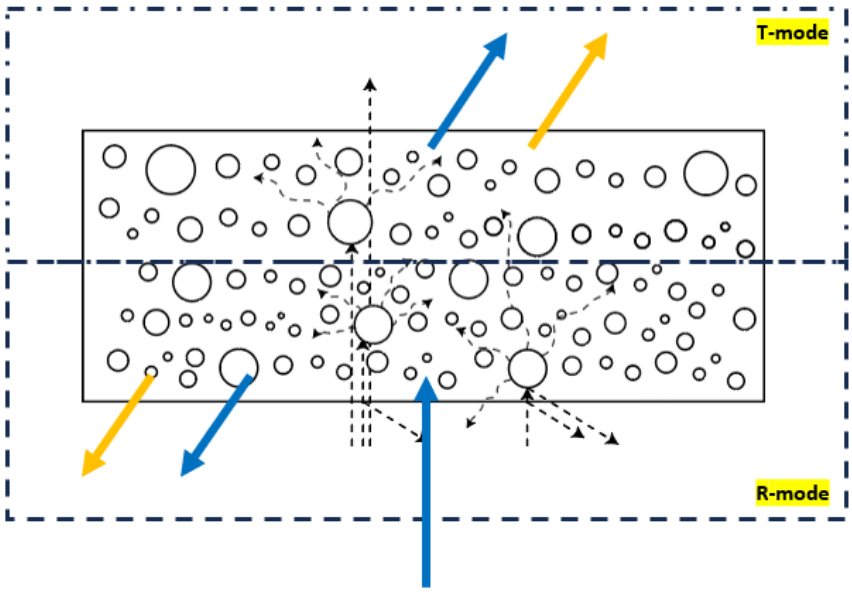

Figure 10. Laser to Phosphor matrix illustration of R mode and T mode (Schur Michael M.).

This means that careful consideration for the geometric design needs to focus around collecting light emitted from the surface the laser subtends to. Figure 11 shows the simulated intensity distribution in polar coordinates. Skipping ahead to Figure 20 in the next chapter, this explains why most LtP devices model like KSLD's SMD, where the R-mode surface of the phosphor is the surface that faces the exit aperture of the LED. Although a model like

Figure 21 is simpler to fabricate, there are many issues that arise discussed in the next section.

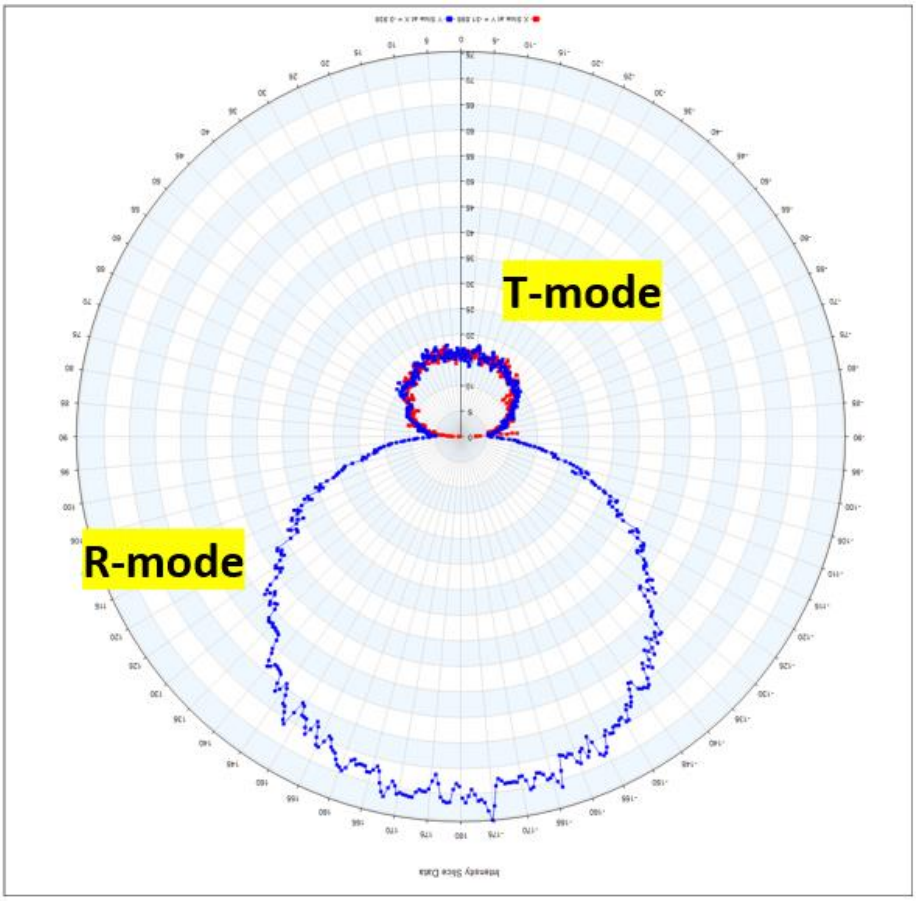

Figure 11. Polar coordinates of intensity slice data for initial simulation results of a 450 nm laser exciting a YAG phosphor (Schur Michael M.).

A Brief explanation of CCT and CIE

There are two color metrics we are concerned with, correlated color temperature (CCT)[14] and CIE color coordinates[15]. Keep in mind these metrics are human derived, meaning that

[14] CCT calculations in LightTools are based on the paper "Computation of Correlated Color Temperature and Distribution Temperature" by A. R. Robertson, JOSA Vol. 58, No. 11, p. 1528, November 1968.

[15] LightTools bases calculations for CIE coordinates on The Lighting Handbook, 8th Ed., Mark Rhea, et al., Illuminating Engineering Society of North America, 1993, p. 109 and Color Science, 2nd Ed.,Gunther Wyszecki and W. S. Styles, 1982, p. 130.

they describe, on average, the perception of color based on the chromaticity of radiation rather than its spectral distribution. We care about this because when creating an LED we also concern ourselves with how the color of the emitted radiation will be perceived. The calculations for chromaticity are based on the spectral density of the observed light which has a matching CIE color function. The function comprises of tristimulus values, normally represented by X, Y, and Z or r(λ), g(λ), b(λ) respectively[16], and are used to create what is known as the 1931 x,y chromaticity diagram (seen in Figure 14) (Angelo V. Arecchi, 2014).

CCT is strictly used when correlating to a white color, the spectral characteristics of blackbody radiation vary depending on its surface temperature. Consequently, a blackbody's surface temperature can help determine the color and spectral distribution of its emitted light, this has a correlating blackbody radiation curve in the central part of the CIE x,y chromaticity diagram. This metric is used to better understand the chromaticity results of our system, wherein cool white light typically has a CCT above 5000 K, indicating a higher intensity of blue tones, while warm white light, with its more orange-red hue, has a CCT below 4000 K.

Using both CIE x,y and CCT we ultimately optimize our phosphor variables to either decrease MFP or increase it. By increasing our MFP we increase the likelihood of phosphor particles down-converting the excitation radiation and therefore increasing the spectral density of our yellow wavelengths tilting CCT below 4000 K towards yellow. Inversely so, if we chose to change variables to decrease MFP we decrease conversion rates and increase spectral density of our blue wavelengths tilting CCT above 5000 K. When using our merit

[16] The human eye has three types of cones responsible our color vision a "blue cone", 420 nm – 440 nm, "green cone", 530 nm – 540 nm, and "red cone", 560 nm – 580 nm. These cones have respective spectral distribution functions that correlate to the CIE tristimulus values.

function to optimize for color we assign the target D65 values, CCT 6508 K, and CIE x,y (0.3127, 0.3290).

We examine excitation wavelength to observe its effect on CCT and generated lumens[17]. The results listed in Figure 12 show that by decreasing excitation wavelength from 455 nm to 445 nm, you increase generated lumen output, increase CCT in R-mode, and slightly

	455 nm		450 nm		445 nm		
CIE	T-mode	R-mode	T-mode	R-mode	T-mode	R-mode	D65
X	0.4391	0.328	0.4378	0.3201	0.4353	0.3088	0.3127
Y	0.5409	0.3675	0.5397	0.344	0.5361	0.3055	0.3290
CCT (K)	3763	5670	3776	6054	3796	6985	6508
Collected lumens	298		332		336		

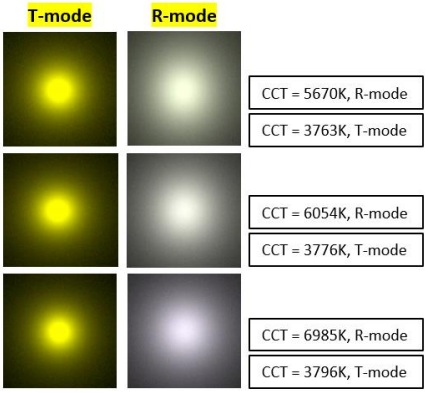

Figure 12. Results of varying the wavelength of the excitation beam. Correlated simulated images to the right, from top to bottom results for 455 nm, 450 nm and 445 nm. White point value of D65 also listed (Schur Michael M.).

increase CCT in T-mode (Robertson, 1968)[18]. Looking back at the previous chapter where we discussed absorption and excitation spectra of the phosphor, the values of 450 nm and 445 nm yield higher collected lumens because they align better to the respective spectral peaks, thus activating more particles to generate more lumens. Herein lies the optical trade off and the optimization that will need to be conducted, optimizing parameters while keeping the fidelity of color coordinates around white (D65) while generating maximal number of lumens.

[17] Varying excitation beam with the same spectral data is not recommended. Spectral data of the phosphor should use the same excitation wavelength used to record it. Results for these wavelengths are assumed to yield a similar spectral curve.

[18] Higher CCT correlates to cooler, 'bluer' values whereas lower CCT values are warmer 'red-er'. CCT is the absolute temperature of a black body whose chromaticity (or color appearance) most nearly approximates that of the light source. LT explains that, CCT also can be a function of position, like illuminance or intensity, CCT calculations are based on the paper "Computation of Correlated Color Temperature and Distribution Temperature" by A. R. Robertson, JOSA Vol. 58, No. 11, p. 1528, November 1968.

The lighting industry continues to use color definitions specified in C.I.E 1931 Chromaticity Diagram, even though there have been multiple updates since. CIE defines several different white points, but one that is used in many testing facilities is the CIE Standard Illuminant D65. This white point corresponds to a CCT[19] of 6,508 K and has an x/y value of 0.3127 and 0.3290 respectively. We map the R values on a zoomed 1931 Chromaticity Diagram to illustrate their relationship to D65 as seen in Figure 13. Ideally, we want a white LED with CCT aligning with D65, with a maximum number of lumens generated. However, it is likely we will trade color for higher luminous output, especially for devices wherein output is more important than color. As observed in Figure 13 as the CCT increases, lumens generated decreases simply due to less down-conversion. The average LE of this system for as close to white point was simulated to be 323 lumens/watt.

[19] LightTools limits the maximum value for CCT at 100,000 K and the minimum value at 1667 K. Values outside this range are generally not of interest for illumination analysis.

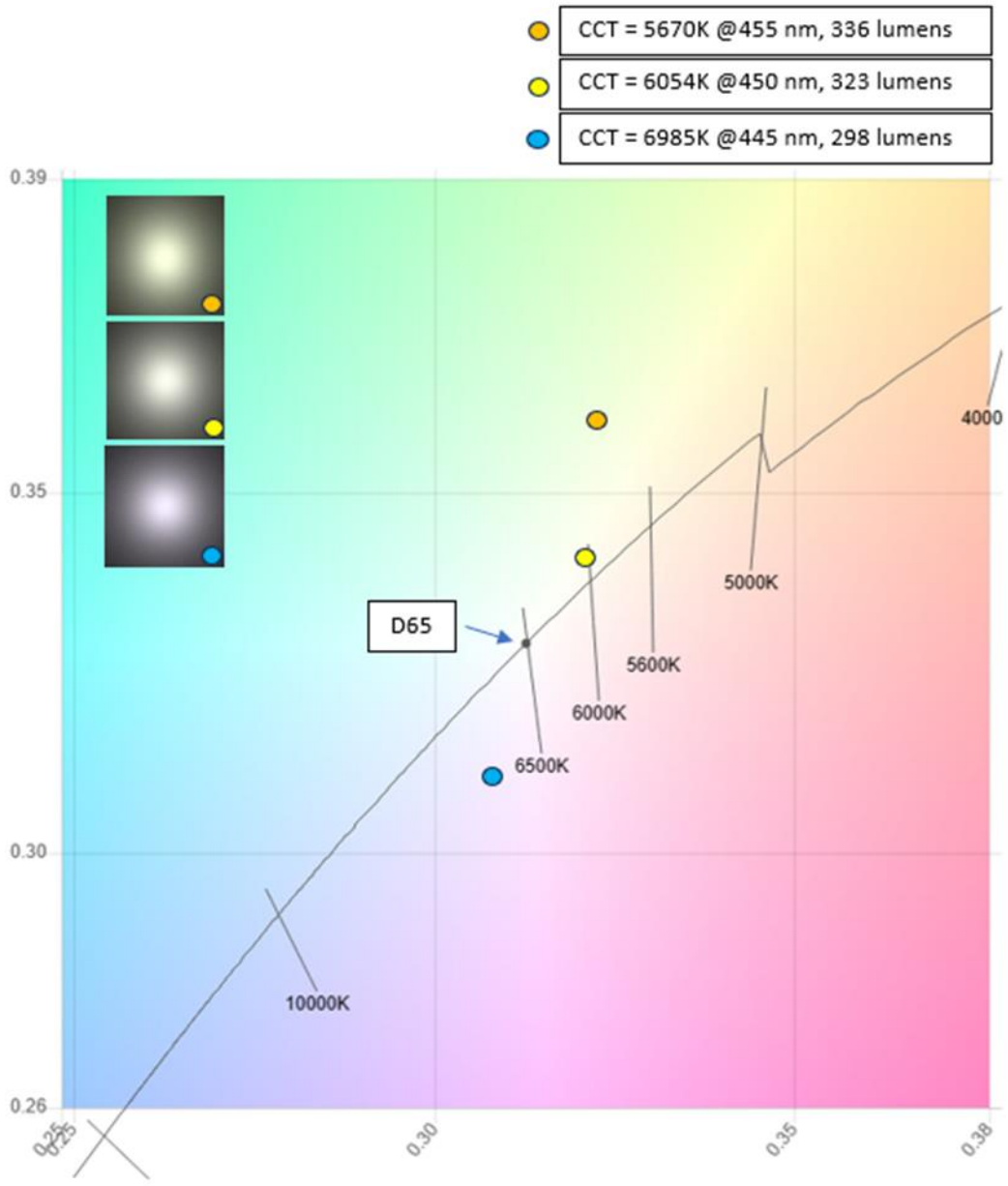

Figure 13. Zoomed up view of the simulated CCT values for varying wavelengths, plotted on a 1931 CIE color diagram. Reference to D65 (Schur Michael M.).

Displays utilize three different colored phosphors within a pixel to control color emission. As represented in Figure 14, the three black points represent each of the three

phosphors[20] red, green and blue, together they create a color triangle wherein the colors

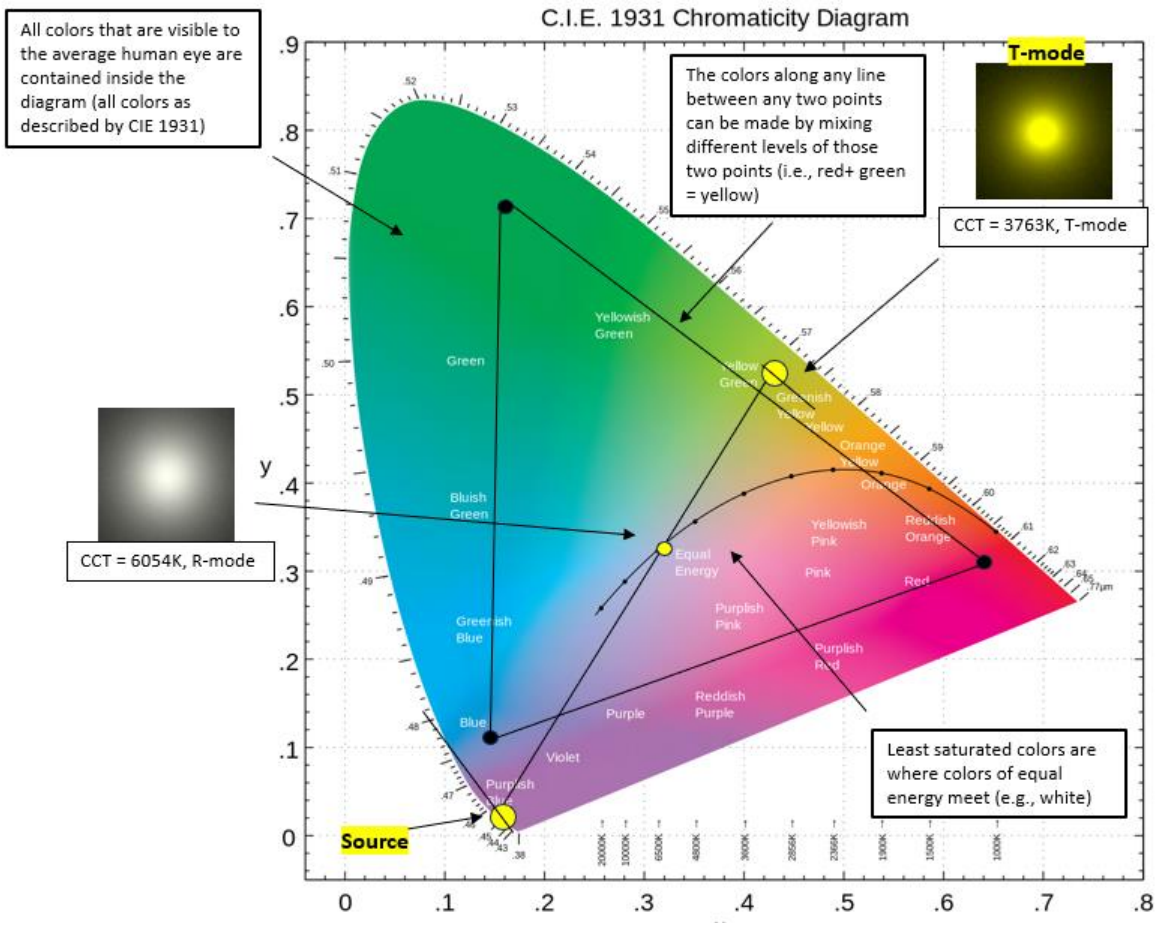

Figure 14. 1931 Chromaticity Diagram, with the 450-nm source and correlating R and T plotted. A line can be generated between them illustrating the constraints for color results by using a YAG phosphor (Schur Michael M.).

within that triangle are colors the display can replicate. For a YAG phosphor, the emission is yellow, and the excitation beam ('source') is blue, when plotted, the line between them represents the colors the LED can generate. Changing the variable properties previously listed, moves our white point along the curve, increasing influence of down-conversion or increasing the influence of the source beam.

[20] Some LED III-V semiconductor materials to generate red green and blue include: InGaN for blue and green, AlGaInP for yellow, orange and red, AlGaAs for red, and infrared, GaP for yellow and green.

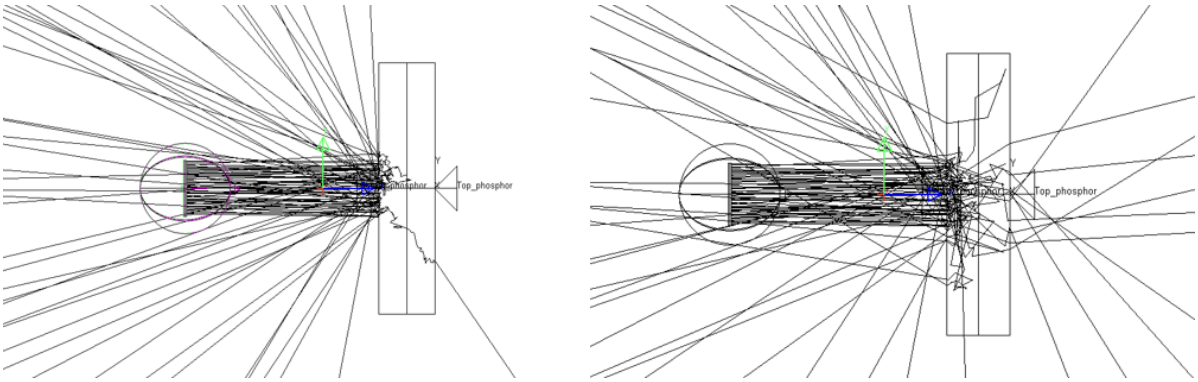

Figure 15. Ray trace using phosphor particles of 1500 nm (left) and 500 nm (right). Higher particle sizes mean that $2\pi r \gg \lambda$ which results in higher reflection and less forward scattering (Schur Michael M.).

In assessing the effects of larger phosphor particles within a phosphor matrix, a ray trace analysis highlighted an increase in the reflectivity of unconverted blue light as the particle size grows. Larger phosphor particles, with their greater surface area, reflect the incident blue light reducing conversion efficiency and consequently lowering the luminous intensity of the source. This change in reflectivity shifts the CIE color coordinates towards the blue end of the spectrum, indicating a more noticeable bluish hue in the output light. The results demonstrated that larger particle sizes (where $2\pi r \gg \lambda$) tend to exhibit higher reflection rates and less forward scattering. This outcome suggests that adjustments to particle size in phosphor matrices can significantly impact light distribution and color. This of course can be modified by reducing the volume percent concentration of the phosphor particles, using larger particles while decreasing volume percent concentration can allow for increased conversion.

Phosphor surface modeling:

Due to the mechanical processing involved in phosphor production—like lapping, abrasive machining, and chemical mechanical polishing (CMP) after sintering—the surface topography of phosphor samples can be modeled with a Fourier function as described by

Lee et al., (Dong-Ho Lee, 2015). The surface roughness affects the blue light emission when it interacts with the phosphor. Currently LT assumes polished ‘smooth’ surface topography, meaning that the ray interacts with the surface as a flat interface. In LT we can change the surface roughness via various methods; with a measured BSDF curve, advanced scattering models or simple scattering models. For these purposes we set the surface to Lambertian scattering.

Sedimentation of phosphor particles during curing:

Particles suspended within a matrix in LT are generally considered to be evenly distributed, but in practice, this assumption might not always hold true. According to the article "Modeling on Phosphor Sedimentation Phenomenon During Curing Process of High Power LED Packaging" by Yiman Wang et al., the authors state that the size distribution of phosphor particles and the time-dependent viscosity of silicone (or a similar material) are critical factors in determining the sedimentation behavior of these particles. As the material cures, viscosity changes, impacting how quickly particles settle. Stokes' law of resistance governs the rate of sedimentation, suggesting that larger or denser particles might settle faster, leading to a higher concentration at the lower part of the matrix due to gravity (Yiman Wang, Modeling on Phosphor Sedimentation Phenomenon During Curing Process of High Power LED Packaging, 2014) . If the phosphor particles accumulate near the base where the

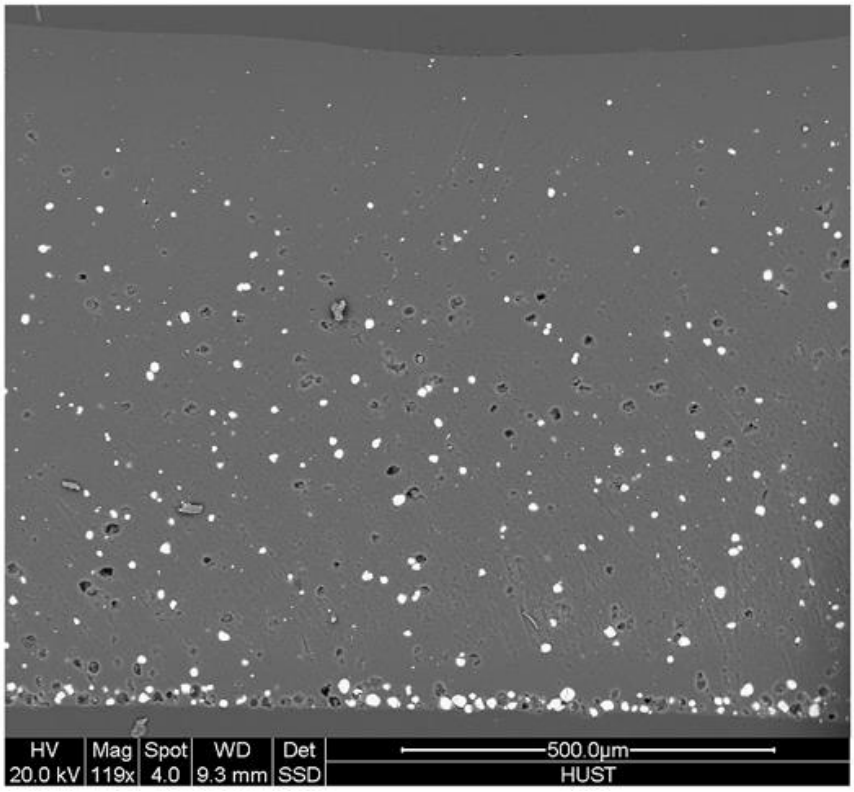

Figure 16. Longitudinal cross-sectional microstructure photograph of sample. Larger phosphor particles observed to sediment at the bottom. Photo taken from Want et al.

excitation laser enters, the phosphors may form a type of reflective layer that diverts the excitation beam away from particles suspended in the medium and therefore reduces luminous output of the system. To simulate we can generate a stack of layers with different concentration of phosphor particles, though as our interest focuses on micro-structures, we considered this negligible without a lab tested comparison.

Lastly, with the points discussed in this chapter we can summarize the ‘feasible’ ranges from current manufacturing processes in the table below to carry them to the next chapter for our optimization merit functions (Linhart, 2022).

Table 2. Optimization variables and their respective initial limitations based on literature review.

Variables	Range
Wavelength	450 nm
Thickness	5-100 μm
Volume%	2-99%
Mie Particle Size	30-1000 nm[21]

B. Simulation II: Inverse Cassegrain

The second simulation builds on the first by placing the phosphor inside an inverse-Cassegrain model. Recall, a 'classic' Cassegrain reflecting telescope which comprises two

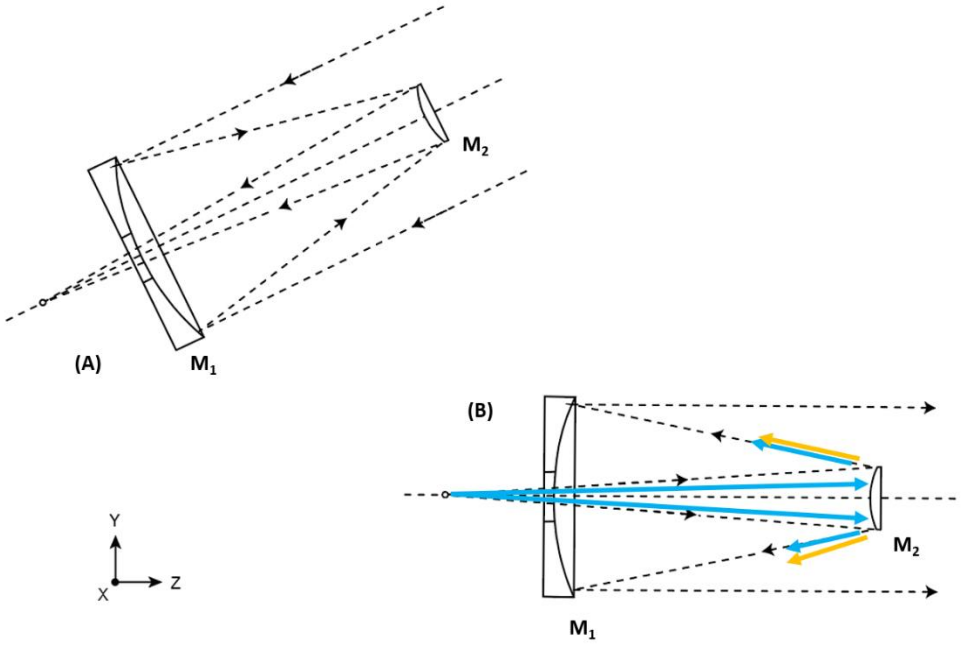

Figure 17. Illustrates the optical path of a Cassegrain and inverse-Cassegrain model. (A), is a 2D cross section of a Cassegrain Telescope with a primary mirror (M_1) and a secondary mirror (M_2). The telescope collects light from the environment and focuses it at a point beyond M_1. Inverting the system (B) shows light emitting from the focal point which falls on M_2 which in this case is a phosphor. Light from the phosphor is collected by M_1 and is collimated out (Schur Michael M.).

mirrors, a parabolic primary mirror (M_1) and a hyperbolic secondary mirror (M_2), seen in

[21] Minimal values taken from (Anne C. Berends, 2020)

Figure 17A (Rosin, 1968). The hyperbolic secondary mirror reflects light collected by the primary mirror and focuses it beyond M_1. Applying the Cassegrainian system for illumination purposes, when it is inversed, a light source starting from the focal point illuminates the secondary mirror (i.e., phosphor). Light emitted by the phosphor is then collected by the primary mirror and collimated out, seen in Figure 17B.

In the theoretical device model as shown in Figure 18A, we apply an inverse-Cassegrain structure (Figure 18B) to a single pixel of an LED. Figure 18A shows a cross sectional view of an LED device (micro or mini) for a singular pixel. At the base of the structure, we have a

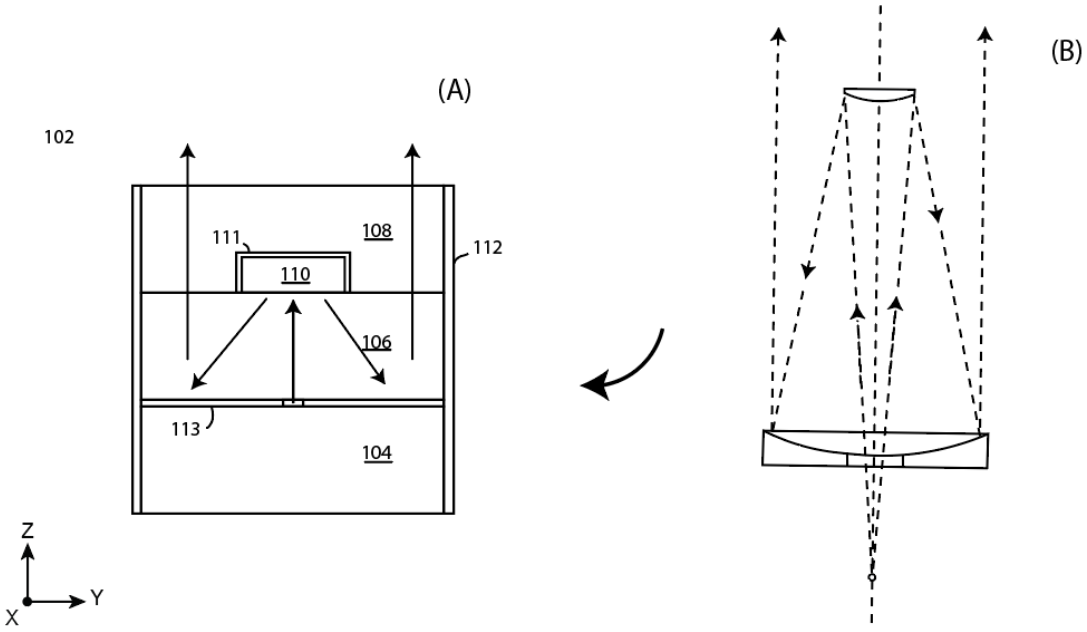

Figure 18. (A) Shows a cross-sectional view initially theorized, of a single segmented pixel for an LED structure when an inverse-Cassegrain model (B) is applied (Schur Michael M.).

light source layer like an ELED stack, a VCSEL or other previously listed in *Simulation I*. On top of that an intermediate layer (106) and a reflective surface between them (effectively acting as a primary mirror), the intermediate layer comprises of an oxide or dielectric material. Acting as the secondary mirror of a Cassegrain model we have a phosphor embedded in the top layer with a reflective coating, to direct light emitted from the phosphor

to the primary mirror instead of transmitting through the phosphor. Lastly, we have a reflective or absorptive coating on the outer perimeter of the stacked device which acts as a deep trench isolation (DTI) (112) and prevents optical crosstalk from pixel to pixel.

Inserting the theoretical device model into the simulation we first need to define the spatial limits of the exit aperture (i.e., pixel surface). Because we are interested in developing a micro-LED we limit the dimensions of the pixel to be less than the upper limit of a micro-LED (<100 μm). LED sizes are typically understood to fall under three categories: micro, mini, and 'standard'. Micro-LEDs (μLEDs) have end-to-end dimensions ranging from a few microns to 100 μm. Mini-LEDs are slightly larger, with dimensions ranging from 100 μm to a few hundred microns. 'Standard' LEDs, have an average size of approximately 1000 μm (Mertens, 2024).

Upon selecting size limitations, choosing a reflector shape to use as our primary mirror is the next step. The first mirror structure we evaluated was a CPC (compound parabolic concentrator) seen in Figure 20. CPCs are used to concentrate the radiation from a clipped Lambertian source in a nearly étendue-preserving manner, wherein the Lambertian source spans along the entrance aperture aimed at the exit aperture (Bass, 2010). This

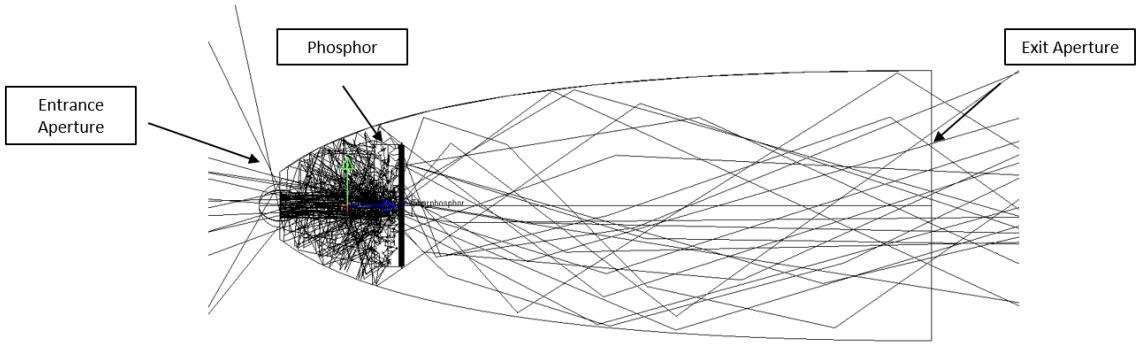

Figure 19. Shows a CPC reflector with a phosphor inside with rays emitted from the excited surface of the phosphor lost (Schur Michael M.).

system was quickly dismissed, as we realized that an efficient LtP system needs to collect and mix light off the R-mode surface of the phosphor. In *Simulation I* recall the results

illustrating that the greatest amount of flux is generated off the R-side of the phosphor. It is

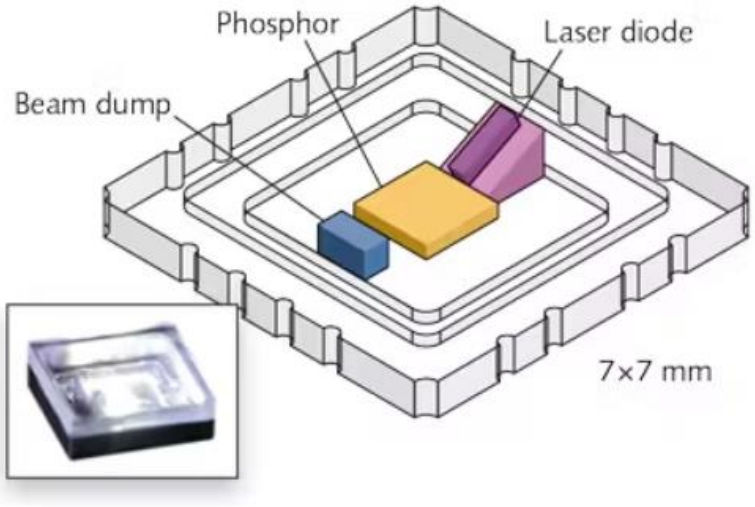

Figure 20. KSLD's LtP SMD system, using the R-mode surface of the phosphor (Overton, 2017).

postulated, that because of this physical feature, most LED manufacturers for LtP systems will focus designing their products as a surface mounted device (SMD), pictured in Figure 20. SMDs simply use the excited surface of the phosphor for direct emission (Overton, 2017). Though SMDs may be simpler to manufacture, the system itself has many optical trade-offs including lower conversion, and virtually no capacity for color mixing, or beam shaping, later discussed in this chapter. The example in Figure 20 comes from patent US10879673B2 filed by Soraa Laser Diode Inc in 2018 (currently owned by Kyocera SLD Laser Inc) (USA Patent No. US10879673B2, 2018). Our hope is that by using IC geometry we can collect and mix both laser and phosphor lights equating to higher flux and better color uniformity while shaping our beam to have narrow emission.

The second shape considered for the reflector was a conic reflector, several conic constant values were evaluated and among them two were selected for further optimization. Optical systems benefit from being rotationally symmetric about the z-axis, one design

feature in LT is the ability to generate rotationally symmetric surfaces simple or polynomial via conics and/or super conics. A conic surface is defined by a radius (r) and a conic

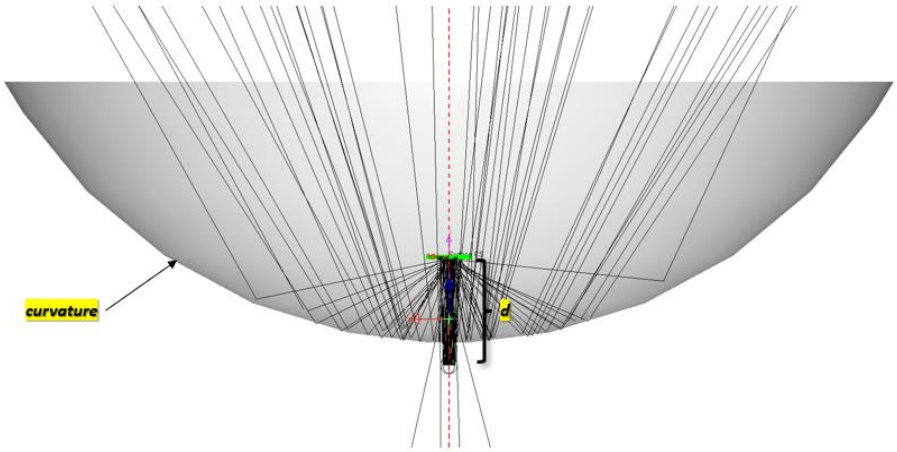

Figure 21. Illustrates LT's simulation set-up for a LtP system using a conic reflector (Schur Michael M.).

constant (k), the conic constant refers to the type of surface which are:

$-1 < k < 0$ ellipse

$k = 0$ sphere

$k = -1$ parabola

$k < -1$ hyperbola

$k > 0$ oblate sphere

the equation used to calculate the sag of a conic surface (z) is given below,

$$z = \frac{cr^2}{1 + \sqrt{1 - (1 + k)c^2r^2}}$$

where c is the surface curvature (1/r), assuming the major axis is the Z-axis (LightTools, 2024). For higher order and greater control LT offers superconic surface control (i.e., aspheric surfaces) (Kumler, 2001).

Four reflectors with the conic constant of -1, 0, 1, and 0.499 were evaluated, and a front projection efficiency (FPE) was calculated to determine which two to further investigate and

optimize, FPE is the ratio of front collect lumens in a 30° x 30° detector to lumens collected in a full 360° detector. Due to better performance and manufacturability, 0 and -1 were selected for further study. The results for optimizing a spherical reflector as seen in Figure 22 demonstrated a slight shift in color coordinates, towards a bluer white, and an increase in FPE. The optimization was done via LT's merit function wherein the optimized variable was the curvature of the reflector to the central intensity of the detector.

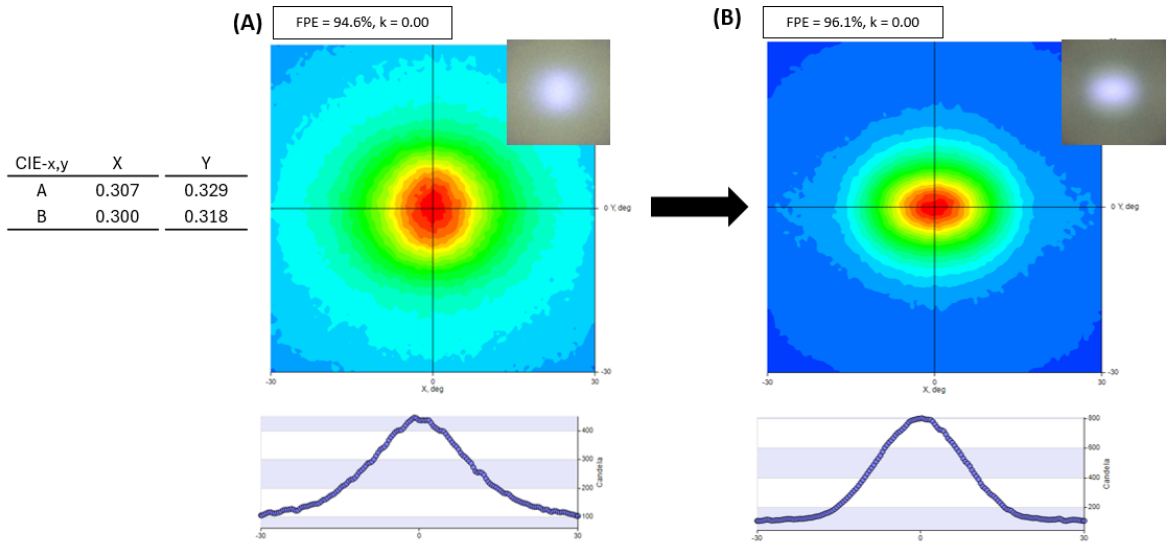

Figure 22. (A) is the initial result of the reflector system before being optimized by LT's merit function for central intensity. (B) is the optimized result, change in curvature.

A similar optimization was done for k =-1 the results of which are in Figure 23, a parabolic reflector for a micro-LED proved to have a much higher max intensity ~2500 cd vs. 800 cd, with the respective lumens for both being 282.56 lumens. This difference led to the design decision to keep the conic constant as -1 throughout the experiment while noting that others may be used for different purposes.

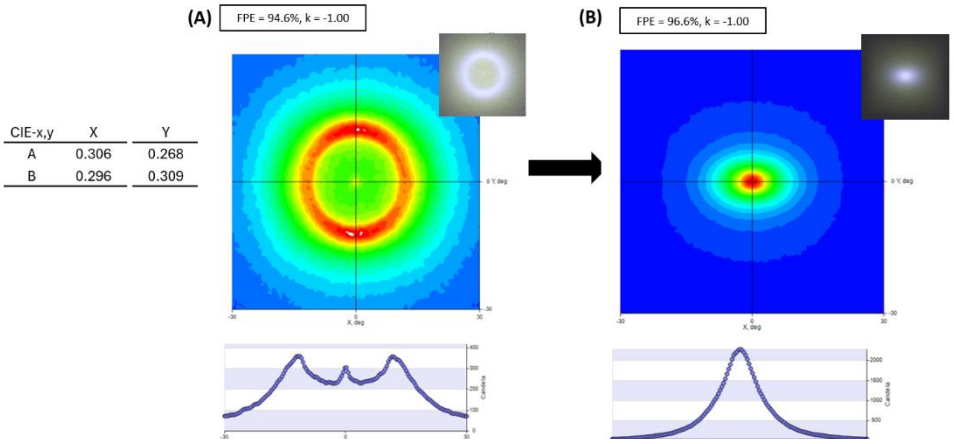

Figure 23. Preoptimized results for k=-1 expressed in segment (A). Optimized results in (B), showed significant shift in avg CIE color coordinates and FPE (Schur Michael M., 2024).

Metallization, to apply a reflective coating, is a common operation in semiconductor fabrication, a highly reflective layer is disposed on top a segmented phosphor chip (techniques for which can include physical vapor deposition PVD or chemical vapor

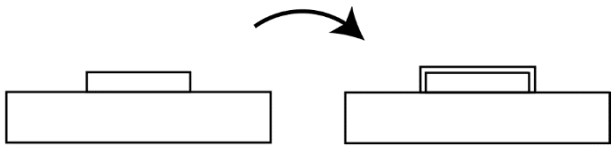

Figure 24. Deposition of reflective layer on phosphor chip (Schur Michael M., 2024).

deposition CVD), as seen in Figure 24 below. These metallic layers can comprise Au, Ag, Al, or an alloy etc. Realizing that we may need to cover the top of the phosphor surface to

prevent direct transmission of laser light to the observer, we simulated the effects of metalizing the phosphor with highly reflective ~98.7% aluminum coating. A metallization layer may act as a barrier for direct viewing of the beam, for beam safety the FDA has four major hazard classification of lasers (I to IV), if the laser is classified above class I, a metallization layer to block direct transmission of the propagating beam is required.

The addition of the metalized layer was simulated and results for metalized vs non-metalized are described in Figure 25. By simply adding the reflective coating to the top of

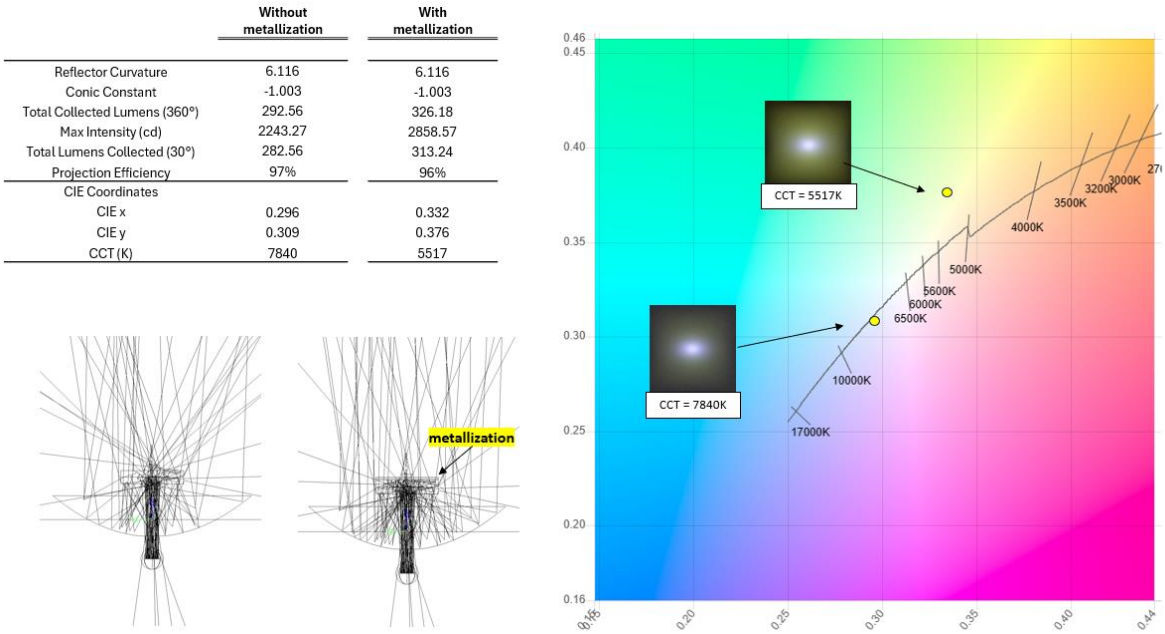

	Without metallization	With metallization
Reflector Curvature	6.116	6.116
Conic Constant	-1.003	-1.003
Total Collected Lumens (360°)	292.56	326.18
Max Intensity (cd)	2243.27	2858.57
Total Lumens Collected (30°)	282.56	313.24
Projection Efficiency	97%	96%
CIE Coordinates		
CIE x	0.296	0.332
CIE y	0.309	0.376
CCT (K)	7840	5517

Figure 25. Comparison of metalized vs non-metalized top phosphor layer for inverse-Cassegrain LtP system (Schur Michael M., 2024).

the phosphor, total collected lumens jumped from 292.56 to 326.18, while CCT shifted substantially from 7840K to 5517K (cooler to warmer). The reasoning behind this significant change is that by adding an aluminum top layer, we are reflecting back into the phosphor matrix unconverted laser light increasing the mean free path of the excitation beam. This increases the statistical likelihood that the excitation beam excites a phosphor particle which results in higher conversion rates (i.e., higher lumen output and yellow light

phosphor emission). This simulation illustrates the optical tradeoff for LtP systems: optimizing for conversion results in an increase of total lumen output at the expense of CCT shifting in the direction of the phosphor emission wavelengths.

In terms of color uniformity, it was noted that obtaining an even color distribution is difficult due to the way each illuminating source propagates: the blue laser, a gaussian beam; the phosphor-converted-yellow, Lambertian. The uneven mixing causes a 'haloing effect' where the center of the white beam may have proper CCT and color coordinate but show obvious deviation towards yellow at wider angles (haloing can be observed in Figure 25). To increase homogeneity of the blue light, one idea was to optimize the surface at which the excitation beam subtends on the phosphor, as shown in Figure 26 below, the angular gaussian

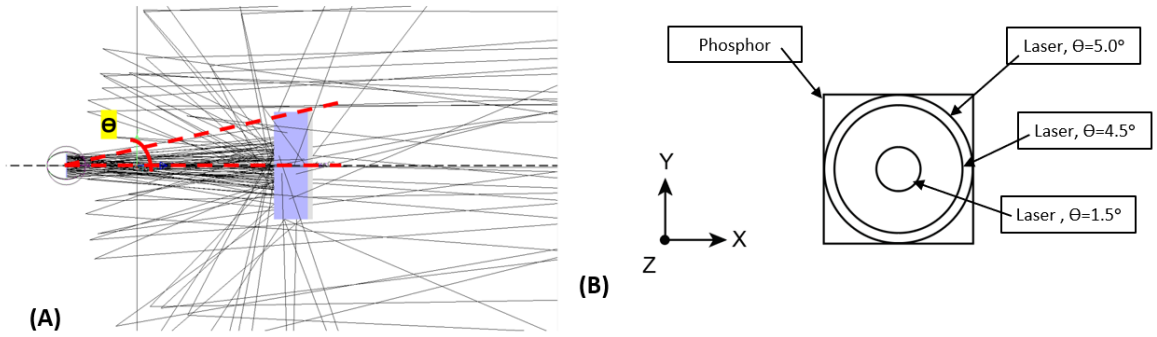

Figure 26. (A) y-z plane view of the laser's angular deviation across the laser, (B) correlating schematic of the surface of the phosphor to which the laser subtends (Schur Michael M., 2024).

distribution was increased from 1.5° to 4.5° in cover a larger surface area of the phosphor. However, the beam should not reach the edge of the phosphor, since there is a chance that the beam will refract inside the matrix without being converted, this will cause blue artifacts in the image which can be viewed when the angle is at ~ 5° (Appendix 1). Though not perfect, optimizing the angle at which the laser subtends the phosphor does create a smoother blue light distribution, as shown in Figure 27. Lastly, these results show when

metallization is done on top of the phosphor, when metallization is performed on the sides, refraction is not an issue and there is no need for a large safety margin.

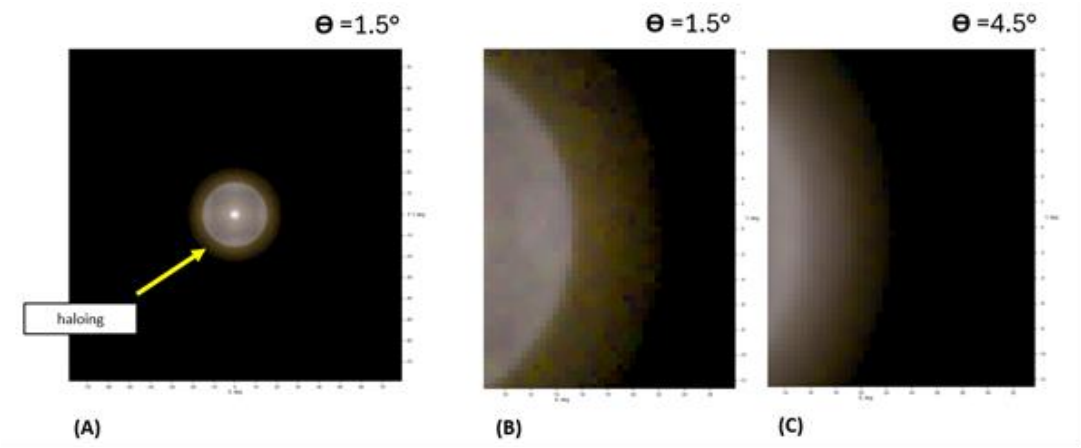

Figure 27. Haloing effect reduced when laser subtends the perimeters of the phosphor. The angular distribution of the laser increased from 1.5 to 4.5 degrees falling towards the edge of the phosphor surface, as referenced in the previous Figure (B) (Schur Michael M., 2024).

Several merit functions were written, in LT, to solve for the following: optimizing variables to yield highest luminous output, beam focusing, color correcting to establish average white color, editing variables to reduce color difference across projected beam. The variables listed can be found in (Appendix 2). Figure 28 shows a detailed result following an optimization.

Variables (Θ = 4.5°)	Values
LUMENS 360 deg	340.7194
MAX INTENSITY 30 deg	13073.27
LUMENS 30 deg	327.3345
CIE X AVG	0.36083
CIE Y AVG	0.413706
CCT (K)	4717

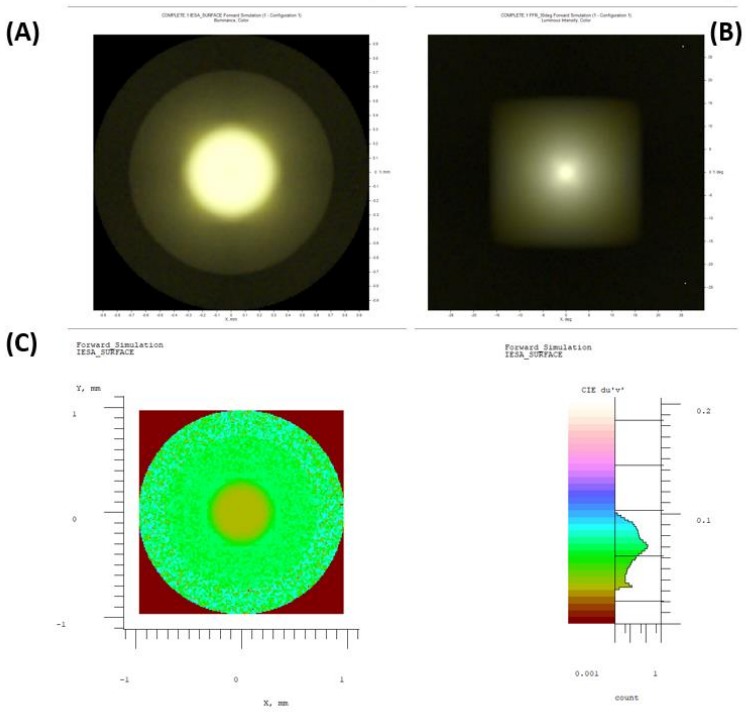

Figure 28. (A) Near-field results placed at the exit aperture. (B) IES type A far-field results. (C) Color difference chart of the near field. Correlating result chart above (Schur Michael M., 2024).

Currently, all the simulations conducted are done in air, however this is not a realistic representation since we can't magically suspend the phosphor inside the reflector. A method for building the inverse-Cassegrain configuration may include a combination of MEMS and semiconductor manufacturing techniques. The methods may include techniques such as EPI-Wafer reconstitution process (EP&T, 2024) or wafer reconstruction both of which are used to form a monolithic wafer for die-to-wafer assembly. A common example of such process is embedding materials in epoxy molding compounds (EMCs) (Wang, et al.,

2013). Using this process, reconstituting singulated phosphor dies inside a substrate allows us to form stackable layers to build the micro-LED. Typically, an LED would need electrical interconnects to allow electricity to excite the phosphor causing it to luminesce, for LtP system there are no need to connect the phosphor to an IC controller and therefore we only need a few manufacturing process steps to generate a component for an LED configuration (micro or other). Therefore taking Figure 17 of the theorized LED configuration, we apply take-aways from the simulation results discussed in this report in order to construct a micro-LED that may look similar to the cross-sectional image of Figure 29.

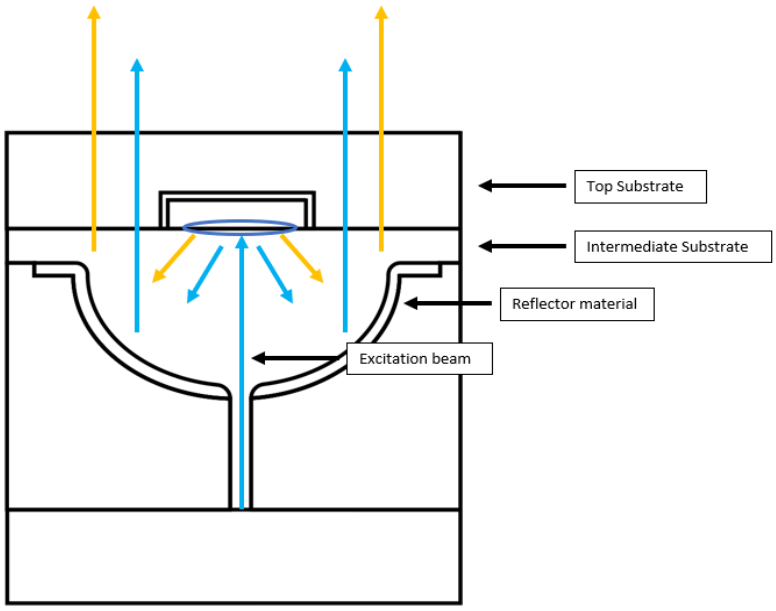

Figure 29. Cross-section schematic overview of a single LtP LED (Schur Michael M., 2024).

Using LT's immersion manager, we replicate the geometry reflected in Figure 29 to align with simulation and test several materials to that the LtP system is embedded in, results for which are found in Table 3 below.

Table 3. Simulated results of using various reconstructed materials.

Name	SiO_2	Air	Silica	PC	Silicone
LUMENS 360 deg	285	293	284	285	284
MAX INTENSITY 30 deg (cd)	4757	10611	5203	4409	5442
CIE X AVG	0.31	0.31	0.31	0.31	0.31
CIE Y AVG	0.33	0.33	0.33	0.33	0.33
LUMENS 180 deg	229	225	229	229	230
CCT (K)	6497	6469	6499	6491	6499
CIE X (@0)	0.29	0.28	0.29	0.29	0.29
CIE Y (@0)	0.27	0.27	0.27	0.27	0.27

Reconstructing the phosphor in a substrate we observe higher scattering, more

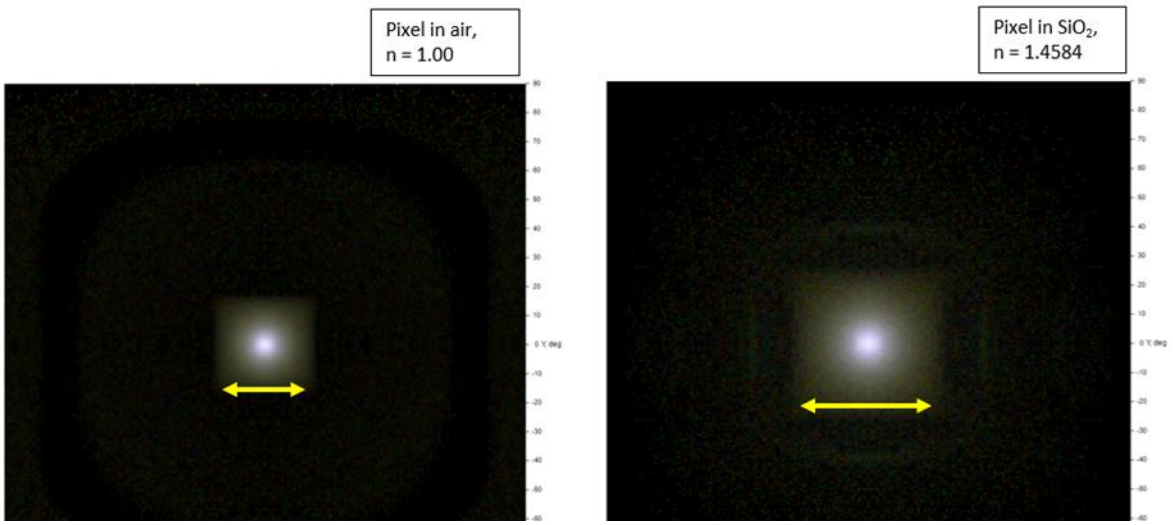

Figure 30. Far field spectral results of when the pixel's environment is in air vs SiO_2 layers. A larger spread is observed as the refractive index causes larger refraction angles (Schur Michael M., 2024).

conversion (CCT slight shift to yellow), and a decrease in lumens and max intensity, as light is absorbed by the material. Reconstructing the system in glass, for example, as illustrated in Figure 30 shows higher a wider attenuation of the beam due to the higher

refractive index of the reconstructed material, the higher the refractive index the less intense the beam will be, which requires a re-optimization of the curvature of the reflector.

Reconstructed stacked surfaces offer numerous benefits. For instance, if the phosphor layer, situated atop an intermediate layer that houses the reflector, depletes, or burns out, the top substrate can be replaced without needing to reconstruct the intermediate layer. Secondly, additional layers or optical films may be stacked in-between or on top to attenuate desired wavelengths, some examples may include adding layers for polarization, additional scattering, wavelength filters, and/or refractive surfaces. Additionally, stacking a meta-lens layer as described by Chen et al. (Mu Ku Chen, 2021) on top of the current configuration may assist in color uniformity while also focusing the multi-spectral beam, without increasing the color difference data across the beam.

A review of literature suggests that the most practical method for addressing color uniformity issue is by introducing a secondary phase in the phosphor matrix, whereby the phosphor matrix is a ceramic. Deng et al reports that when doping a phosphor ceramic with a secondary phase (i.e., TiO_2, BN, Al_2O_3 or SiO_2) you optimize the microstructure of the phosphor to enable higher scattering for blue light excitation. Deng reported that among secondary phases tested, TiO_2 proved to have the best, "multinational uniformity in illumination image, speckle image, illuminance curve, CCT and luminance distribution, followed by BN and $Al2O_3$" (Taoli, 2022)[22]. Doping the phosphor matrix with an additional,

[22] I was interested in simulating the results and adding TiO_2 Mie particles, however, was unsuccessful in obtaining better color mixing, as defined by the article. This may be to lack of material definition. No further investigation was conducted.

inert (non-luminescent) material can be studied further, but it is suggested to parallel this study with concurrent lab results to validate assumptions of the simulation.

Table 4. Results of changing the primary reflector from specular to Lambertian.

	Specular 100%	Δ D65	Lambertian 100%	Δ D65	Specular 90%	Δ D65	Lambertian 90%	Δ D65
LUMENS 360°	299.37		300.61		226.97		209.7	
Max Intensity (cd)	6696.17		92.5		5662.22		66.8	
CIE X AVG	0.318	0.0053	0.32	0.0073	0.315	0.0023	0.317	0.0043
CIE Y AVG	0.336	0.007	0.341	0.012	0.33	0.001	0.335	0.006
LUMENS 180°	274.65		229.17		213.35		164.14	
CCT (K) AVG	6156.6	351.4	6042.66	465.34	6372.89	135.11	6219.9	288.1
CIE X Center	0.289	0.0237	0.288	0.288	0.288	0.288	0.28	0.288
CIE Y Center	0.286	0.043	0.365	0.365	0.285	0.365	0.36	0.365

An alternative suggestion to generate better color mixing is to increase the Lambertian scattering by changing the reflectivity type of the primary mirror to Lambertian instead of assuming a specular reflective coating. The charts, in Figure 31, show that both the near field and far field exhibit good color mixing with low dudv values. It was observed that

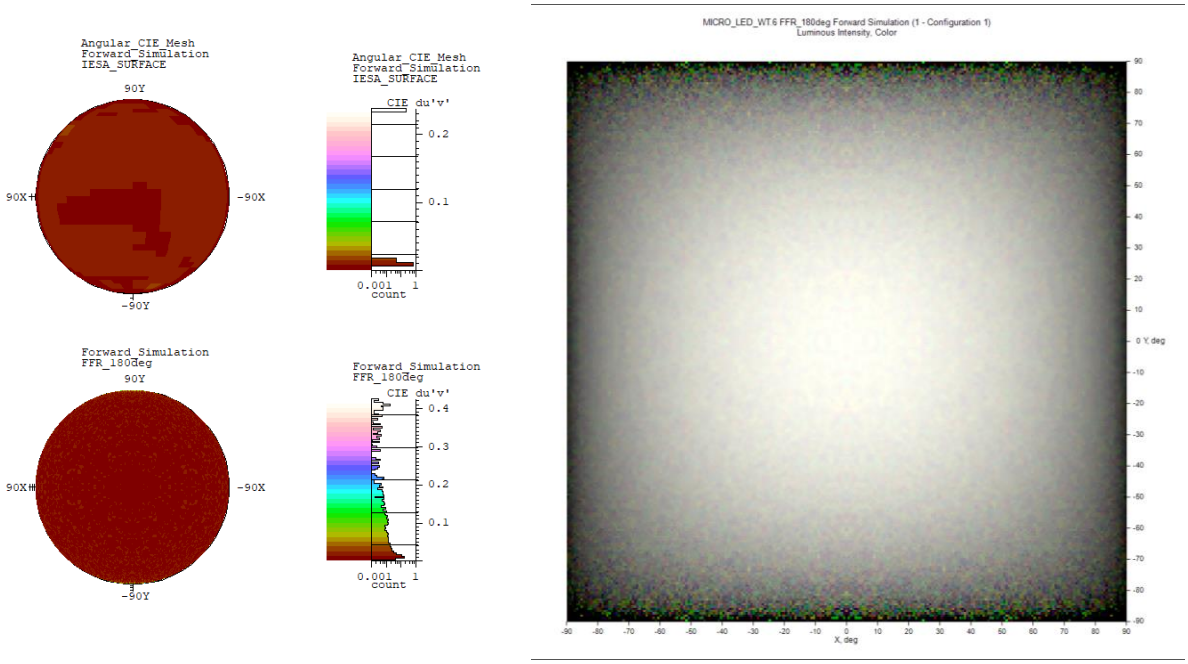

Figure 31. Far field spectral results in a 180 deg sensor above the LED with correlating color difference chart (left bottom) and near field color difference chart (left top). Both results showing good color mixing with low dudv values (Schur Michael M., 2024).

making the reflective coating on the phosphor Lambertian had a much smaller impact on increasing color uniformity, most of the mixing comes from the primary reflector. Values for each simulation with their respective percent reflectivity are listed in Table 4. It should be noted that each system's phosphor composition can be optimized to compensate for the reduction in luminous flux, meaning that we may be able to extract more lumens out of the system by optimizing our phosphor variables previously discussed at the cost of shifting CCT towards the emission spectra.

C. Simulation III: Lucid Shape ADB system

With the current optimized configuration, a 1 million and 50 million .ray file was exported out of LightTools® and converted into LucidShape (LS) binary. LS is the common design software in automotive lighting so to successfully apply the micro-LED in a larger optical system in LS means a potential avenue for distribution of such desired rayfiles. Additionally, LS has many resources to create an ADB system which are utilized in this chapter.

There are four leading technologies for ADB systems in use: pixelated µLEDs, LCDs, DMDs, and optical scanners. The first is a pixelated phosphor LED like OSRAM's µAFS (OSRAM, 2024) (adaptive front-lighting systems), this system uses a blue LED with a pixelated phosphor coating. The second, is an LCD system composed of a LED light source, an LCD screen, and a projection lens (STANLEY LTD, 2024). The third is a digital micro-mirror device (DMD) with digital light processing chips (DLP) illuminated by a high intensity light source. The fourth uses piezoelectric actuation mechanisms for its biaxial MEMS optical scanner and a laser to control how light is distributed on a phosphor plate (Tomotaka Asari, 2021). The IC-LtP system configured in this thesis is comparable to either

the µAFS or the laser-scanning MEMS device, both are additive image sources meaning that a blue light source excites a yellow phosphor to generate white light, however each have comparable differences. The LCD and DMD systems are both subtractive systems, meaning that the source is already a white color, an LCD system will absorb light pixelated from the image plane whereas DMDs will reflect light. It may also be of interest that in addition to DMD systems spatial light modulators (SLMs) have been discussed as alternatives and or additions to DMDs.

Using LS we will take a typical ADB lens system (supplied by LS's model gallery) and evaluate and compare OSRAM's µAFS to the IC LtP LED system. Using the tutorial inside of LS discussing PixelLight (their tool for creating a micro-LED array) we first generate a 32x32 pixelated light source for the µAFS with size and spacing listed previously. This was surprisingly simple and fast for the software to do because the µAFS is assumed to be a Lambertian surface emitter not comprising spectral information. However, that changes when using a .rayfile, for emission information, this caused the system to lag and crash which became difficult to manage, therefore we reduced the size to a 10x10 source when evaluating the IC LtP LED.

For HB HD ADB, we require that the FOV for X and Y respectively are 32° by 8° as illustrated by the mapping in Figure 32—this is for a single headlamp (a LH headlamp having an overlap with a RH headlamp). OSRAM's Smartrix HD setup which uses 4 µAFS

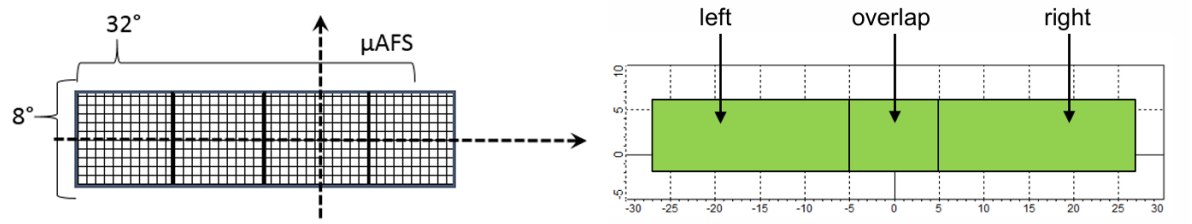

Figure 32. OSRAM's Smartrix HD pixelated FOV map for ADB systems, given by LucidShape's User Guide on PixelLight (LightTools Handbook).

chips (per side) comprises of a two-projector unit (per car lamp), having two chips each in a single headlamp projector configuration. Upon simulating one chip in the projector system, we find one 32 x 32 chip resolves to an 8° x 8° box in the far field image plane, the results of the simulation in Figure 33. This fits precisely inside the LH requirement when 3 more chips are added as outlined in OSRAM's HD HB ADB configuration.

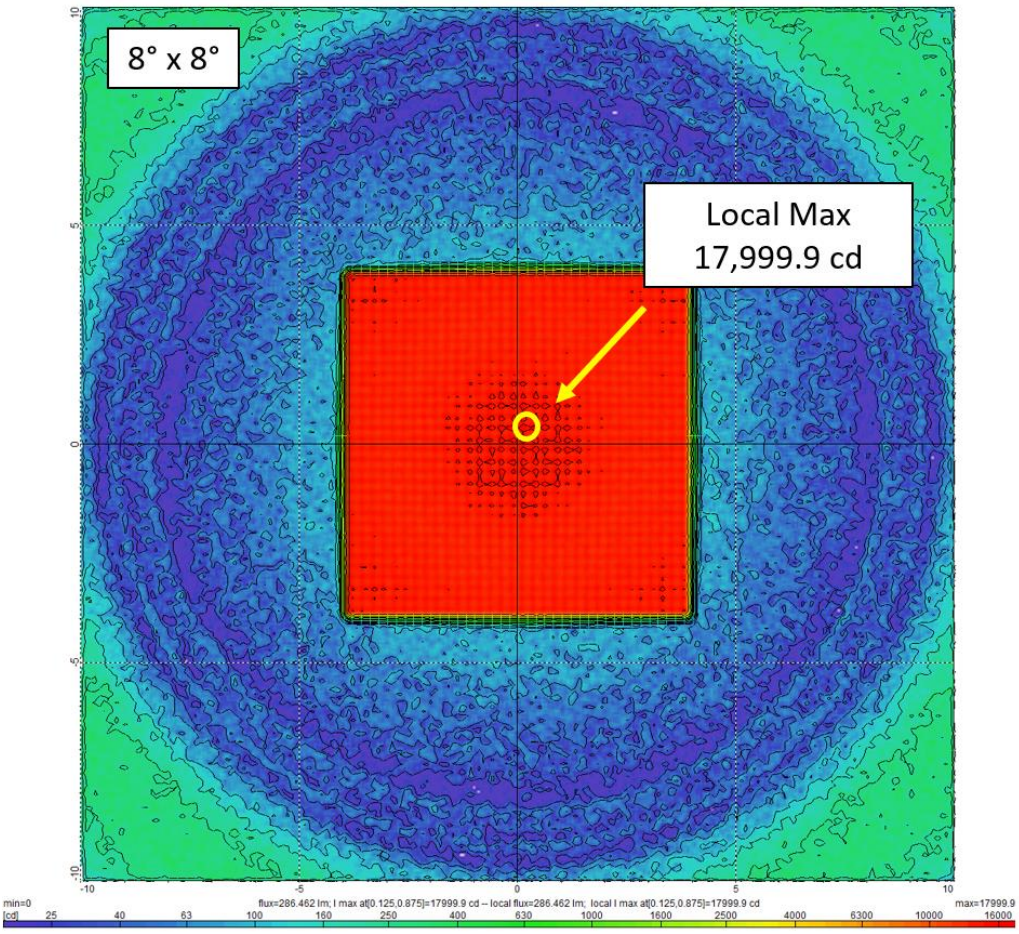

Figure 33. Simulation results (far-field) of a single µAFS chip 32x32 pixel array. Results displayed in a logarithmic scale, false color map (Schur Michael M., 2024).

For this same ADB projector lens model, PixelLight was used to generate a 10x10 array with emission ascribed by the .rayfile. This configuration resulted in a projected FOV of 2° x 2° which fits into OSRAM's requirements for HD. The table of the simulated and calculated results shown below are for a 4mm x 4mm emission surface area where the (1W) system is the max theoretical for the LtP system, the results were also simulated with a 0.1 W laser and simulated, listed in Table 5 below. The LtP system shows a higher projection efficiency due to the emission type, the LtP system also has a higher resolution due to its size, in an emission area of 4-mm x 4-mm Osram can fit 1024 controllable pixels whereas the LtP system can fit 1521 pixels.

Table 5. µAFS systems results compared to the LtP-µLED (1W) and a reduction of 0.1W.

	µAFS	LtP-µLED (1W)	LtP-µLED (0.1W)
Pixels per 4x4 chip	1024	1521	1521
Pixel size (µm)	115	98	98
Spacing (µm)	10	5	5
Lumens per pixel	1-3	229.502	22.95
Emission Type	Lambertian	Gaussian	Gaussian
Lumens/chip	1,024	349,073	34,907
Efficiency	28%	63%	63%
Simulated Lumens	286.46	14,312.10	1,431.21
Simulated I max (cd)	17,999.90	14,240,900	897,055.12

The LtP was simulated using the 10 x 10 configuration then normalized to a 0.1W laser source per pixel to show results. Understanding that there is more room to decrease the laser source power consumption due to heat or general electrical constraints. The far field intensity results shown in Figure 34. Scaling the 10 x 10 configured results to fit into the HD

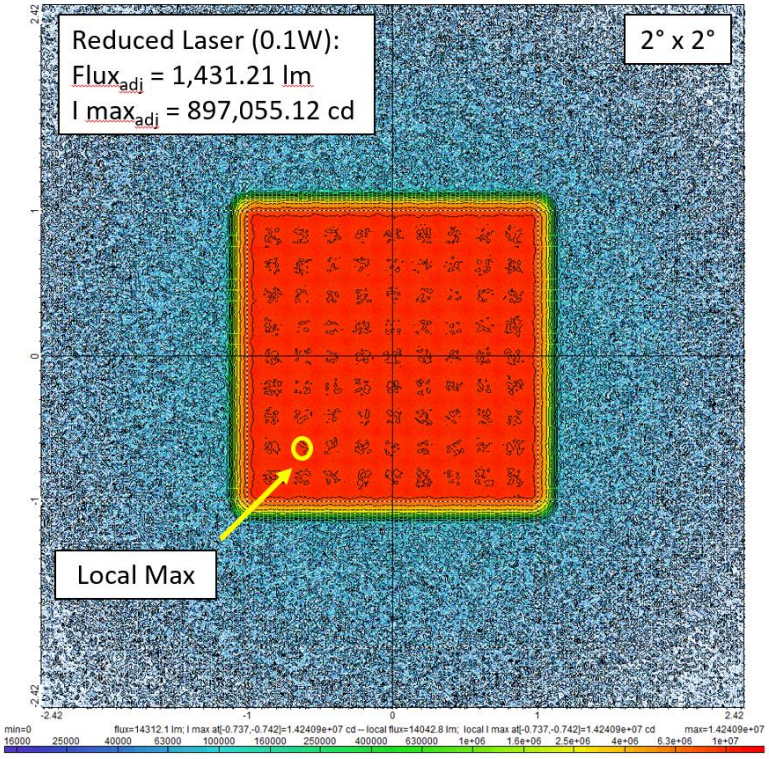

Figure 34. Far field results for the simulated LtP-µLED (1W), scaled to 0.1W. Results displayed in a logarithmic scale, false color map (Schur Michael M., 2024).

FOV, we calculated that in the x direction across the HD ADB map 160 pixels may be individually controlled as compared to OSRAM's µAFS 128, this results in the LtP- µLED having a higher angular resolution of 0.20 degrees an increase of 0.05 degrees as compared to the simulated µAFS results, the values for the resolution of the results shown in Table 6 below. Aside from comparing spectral distribution and color uniformity which we omitted due to being unable to accurately simulate spectral information of the µAFS without lab

Table 6. Simulated resolution results for the μAFS and LtP-μLED.

ADB	μAFS	LtP-μLED (1W)	LtP-μLED (0.1W)
Resolution x (px)	128	160	160
Resolution y (px)	32	40	40
Resolution	4,096	6,400	6,400
Angular resolution	0.25	0.20	0.20

verified results, the next it so projects the systems results on a 25m Illuminance map to measure lux values. For this HD ADB HB we require a minimum of 32 lx per headlamp, the simulated results for lx requirements for μAFS and LtP- μLED are listed in Table X below. For a single μAFS chip, we simulated 28.8 lx, per headlamp was found to be 115 lx and compared to OSRAMS online results of 110 lx, this showed good correlation between our simulation and values reported online. The results under LtP- μLED were a combination of simulated and then normalized results, the 10x10 chip was simulated to have 61.577 lx however these fits in 1 32x32 μAFS FOV 16 times resulting in 985 lumens in a direct size comparison. This was also done to the simulated results at 0.1 W laser beam source.

Table 7. Simulated illuminance results for the μAFS and LtP-μLED.

Illuminance @25 m	μAFS	LtP-μLED (1W)	LtP-μLED (0.1W)
Simulated per chip (lx)	28.8	985	59.1
Simulated per headlamp (lx)	115	3941	236.5
Reported (lx)	110	NA	NA

III. Discussion

IC-LtP LED systems show potential improvements over traditional systems with higher resolution, better output efficiency, and uniform color mixing. Once more, the method in which these may be manufacture via layer stacking, offers more flexibility to customize LED chips without the need of increasing manufacturing costs. For example, the primary mirror layer can be manufactured in monolithic wafer sets and in bulk for both automotive

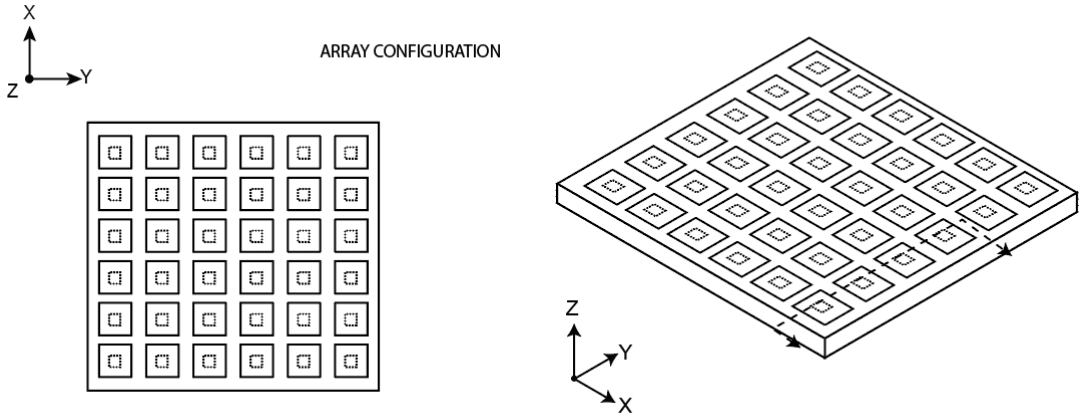

Figure 35. Schematic of a LtP-µLED chip (Schur Michael M., 2024).

and display LED chips, the difference would be to bond a different top and bottom layer. As the device currently stands for ADB HD systems an array configuration of IC-LtP LED pixels is likely to be used as illustrated by Figure 35. The sizes of the pixel's emission surface will ultimately be determined by how small a phosphor chip can be made limited by the power density of the laser emission avoiding issues caused by luminance saturation e.g., optical and thermal quenching.

As mentioned, thermal simulations were not conducted, and this thesis would benefit greatly from thermal simulations in conjunction with lab tests to validate the reported

simulation results as discussed herein. A particularly large concern is thermal quenching of the phosphor chip, this causes luminance saturation and prevents the phosphor particles from generating light. When the phosphor is excited by a high-power-density laser the particles not only generate color converted wavelengths but absorb the additional energy creating heat.

A main issue reported with blue laser diodes for LtP systems is that traditional phosphor encapsulation techniques done in organic binders are done so with a lower heat resistance and thermal conductivity in mind (~0.1-0.4 W/ m K). According to the optimized configuration calculated in the previous section the radius of the excitation beam for a μLED configuration would need to be ~5 μm for a phosphor that is 20 μm. Simulations conducted had the excitation beam of the 450 nm laser to be 1W, a reduction in radiometric power of the excitation beam would need to be done to prevent the accumulation of heat. Heat accumulation would cause a sharp rise in temperature around the local light spot area (of which the excitation beam subtends)—thus leading to quenching or beyond that it may create a black dot which is the result of burning material (i.e., carbonization) (Yirong Xu, 2019).

Phosphors, in addition to thermal quenching, can experience luminescence saturation via optically induced quenching. As discussed by Li. et al, “our group found that the internal quantum efficiency of phosphors decreases with increasing incident laser power density even if thermal quenching is circumvented” meaning that independent from thermally induced luminance saturation, the limits of photoexcitation quenching for micro sized phosphors needs to be studied (Shuxing Li Y. G.-J., 2022). Li et al, considers alternative phosphor matrices outside of traditional binders among them being phosphor in silicone

(PiS), phosphor in metal (PiM), single-crystal phosphors (SCPs), transparent ceramic phosphors (TCPs), and phosphor in glass (PiG). The report suggests that TCPs have high conductivity, have a rich microstructure tunability for color mixing, and have excellent reliability. Testing spectral results and emission from TCPs and inserting them into the simulation model should also be studied.

Although the focus was to insert the IC-LtP LED into an ADB projection system the LED can be potentially used for a variety of applications. For example, you may want to create a pixel array for a light bar of a vehicle and realize that μLED sizes are too costly and small for the proposed function. The size of the LED can therefore be expanded to the size fitting the function of user applications, in this example the size may be increased to 300 μm

Figure 36. LtP LED configuration possibly applied to Rivian auxiliary front lighting (boxed in red) or other signal lighting functions such as DRL (Rivian) (Schur Michael M., 2024).

and placed in an external lighting system of a vehicle like an auxiliary lamp or a DRL as highlighted in Figure 36. What's interesting about the customizability of stackable IC-LtPs is that different layers can be replaced with different valued items so long as there is a laser layer, a primary mirror layer and a phosphor layer. Meaning that if a customer wants an LED that emits broader spectra, one only needs to replace the phosphor layer with another

broadband phosphor and exchange the 450 nm blue laser layer with a UV light layer (further simulated below). Some other ideas for application include that the laser layer can be exchanged for an IR layer to be integrated in the car's camera/detection system. The IC-LtP LED systems can also be configured for white light communication as car manufacturers seek to integrate additional imaging components in their lamps.

Reviewing the spectral distribution of the IC LtP-LED, we find it wanting for applications that may require a more photopic spectra (e.g., display applications or other

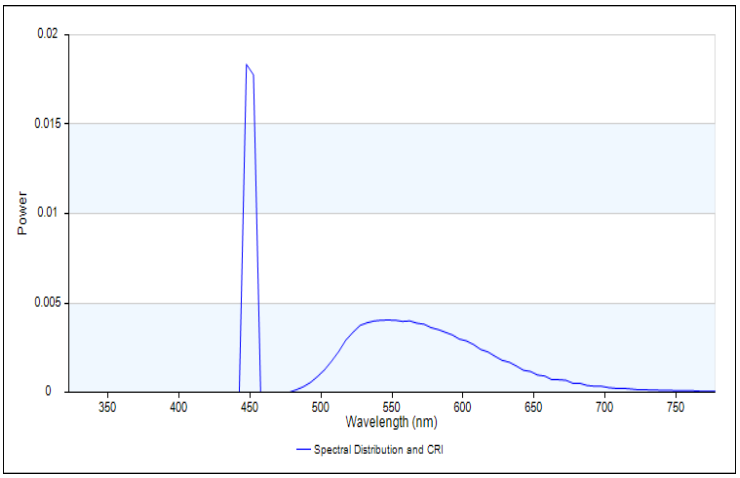

Figure 37. Spectral distribution of the optimized LtP LED using a YAG:Phosphor (Schur Michael M., 2024).

broadband illumination systems). Going back to LT we seek to exchange the YAG phosphor previously studied with an extra-broadband phosphor that would yield a fuller spectrum. Information from "Data-driven Discovery of Full Visible-Spectrum Phosphors" S. Li et al,. for a phosphor comprising $Sr_2AlSi_2O_6N:Eu^{2+}$ was digitized and inserted into the phosphor model, see Figure 38 (Shuxing Li Y. X., 2019). This Sr:Eu phosphor has an absorption in the UV but has emission nearly identical to the photopic spectra. Inside the LT simulation, the excitation beam was adjusted from 450 nm to 330 nm, simulation parameters were adjusted

to include wavelengths of 250-900 nm and the same optimization steps were conducted with the given phosphor material (assumed to be embedded in a silicone matrix), results below:

Table 8. Simulated results for $Sr:Eu^{2+}$ phosphor, inside the IC LtP LED, post matrix optimization.

$Sr_2AlSi_2O_6N:Eu^{2+}$	Values
LUMENS 180 deg	141.50
CCT (K)	3312.64
MAX INTENSITY (cd)	3039.19

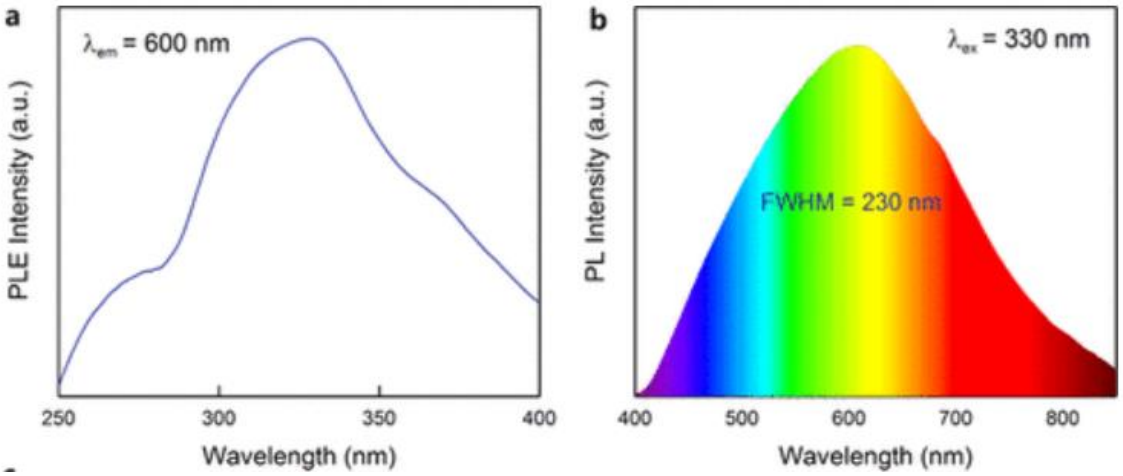

Figure 38. Raw data of absorbance spectra and correlating emission spectra (Shuxing Li Y. X., 2019).

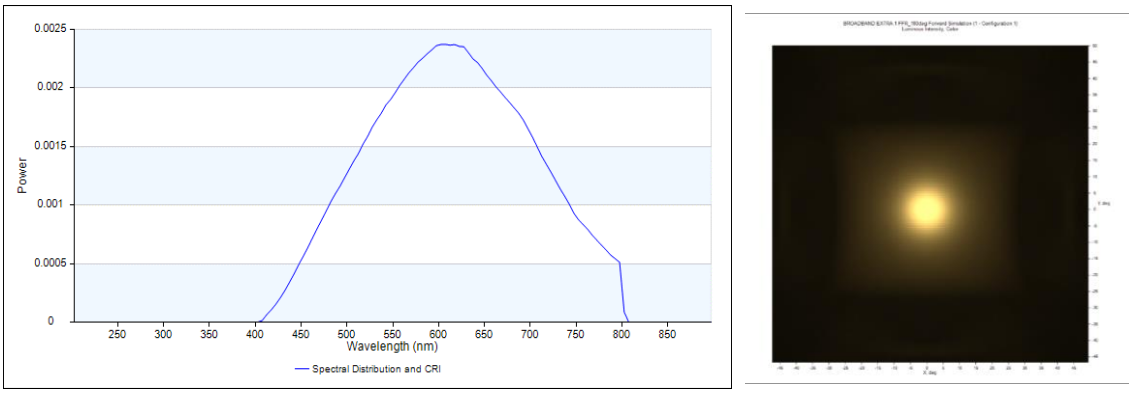

Figure 39. Spectral distribution of the $Sr:Eu^{2+}$ phosphor, inside the IC LtP LED, post matrix optimization with correlating far-field spectral image. Note that at the end of the spectral distribution curve the results end at ~805 nm this is due to digitizing error, wherein the raw results don't continue past ~805 nm (Schur Michael M., 2024).

The spectral distribution of the IC LtP LED when comprising a broadband spectrum shows a broad curve and can result for larger optical applications to have better color rendering properties. Further studies can be conducted to discover proper applications. The same processing can be done for IR generating phosphors, using the absorbance and emission spectra of an Li:Cr^{3+} phosphor. Though, in addition to exchanging the phosphor, a different reconstructed material for the pixel matrix should be considered to efficiently transmit the IR emission beam. Subsequently, IR emitting LtP LEDs may be used and integrated with IR detecting cameras on cars, however further studies should be conducted to validate this claim.

Conclusion

Using standard Cassegrain telescope design, in reverse, we looked at effective methods for phosphor illumination to create white light for automotive applications. Taking the inverse Cassegrain structure we optimize geometry, and phosphor matrix variables to increase lumen output while balancing with desired CCT all confined in a micro-LED package (pictured in Figure 40). We determined that the luminous efficacy of this configuration falls within a range of 295-360 lumens per watt with CCT ranging from 4717 K - 6042K. By reducing specular reflection of components and increasing Lambertian reflection of the mirror and phosphor surfaces, you can reduce the dudv color difference

values to be uniform across the emission beam of the LED but the tradeoff is sacrificing luminous efficacy along with increasing the projection beam angle.

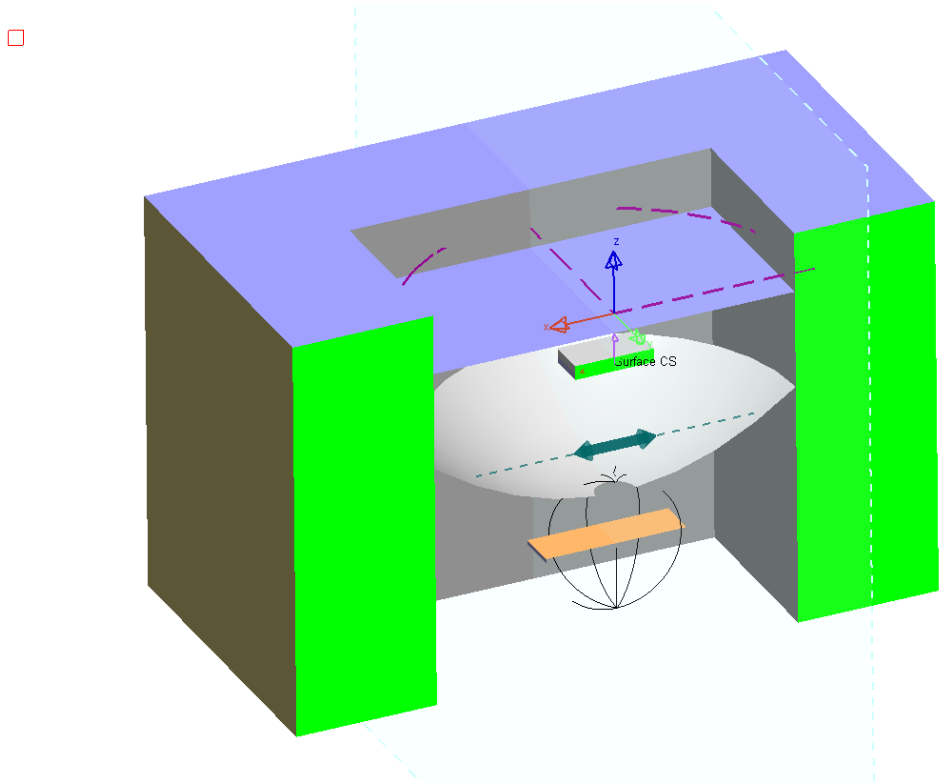

Figure 40. Isometric cross section of final device model in LightTools® (Schur Michael M.).

Understanding this model needed to be suspended in a medium for it to work, we evaluated reconstructing all the components of the inverse-Cassegrain into stackable wafer assemblies. This allows us to generate an IC LtP-µLED chip structure in a 10x10 array, we evaluated the chip and compared it to an industry standard, like OSRAM's µAFS and plugged both into LucidShape's ADB projection lamp. We simulated that the IC LtP-µLED chip is 35% more efficient and can potentially project 5 to 30 times the number of lumens per chip size. We also calculated that the IC LtP system has an increase of 0.05 degrees allowing for more high-definition application and simulated on a 25-m illuminance map to

show that the IC LtP system also has at least two times higher illuminance than the μAFS per chiplet.

As the automotive industry seeks to increase energy efficiency of electrical components IC-LtP LEDs offer a solution to reduce energy consumption without sacrificing luminous output. In a 1:1 comparison normalizing each IC LtP pixel to emit 1 lumen would require only 0.0027 W per pixel and in a 32 x 32-pixel device package the whole chip would need 2.76 W to generate slightly above 1k lumens. This is a huge improvement over traditional devices and therefore may be utilized by other industries that require high luminance sources, like AR/VR displays. Lastly, the stackability of the wafer assembly per part-layer allows you to keep IC-LtP geometry while exchanging either the reconstructed phosphor layer and/or the excitation layer to customize spectral output for a variety of applications. We briefly discussed that by replacing the YAG phosphor with a broadband phosphor or an IR phosphor the IC LtP LED can be used to emit broadband spectrum of light or IR.

Solid-state lighting is an exciting field that integrates knowledge from multiple disciplines, including electrical engineering, chemistry, and optical sciences. As we seek to increase the energy efficiency of our systems, there is ongoing interest in further optimizing phosphor variables for solid-state lighting. Future research directions may involve exploring novel materials and how to effectively simulate those materials. For example, instead of using a simple YAG phosphor layer in LightTools®, there is a growing need to develop accurate simulation techniques for more complex materials such as quantum dots or phosphor nanoparticles embedded in ceramics. By advancing our simulation capabilities to accurately model these advanced materials, we can gain deeper insights into their optical

properties and unlock new possibilities for enhancing the performance of solid-state lighting systems.

IV. Possible Manufacturing Steps for the IC LtP LED

Stackable Micro LED based on an inverse Cassegrain model.

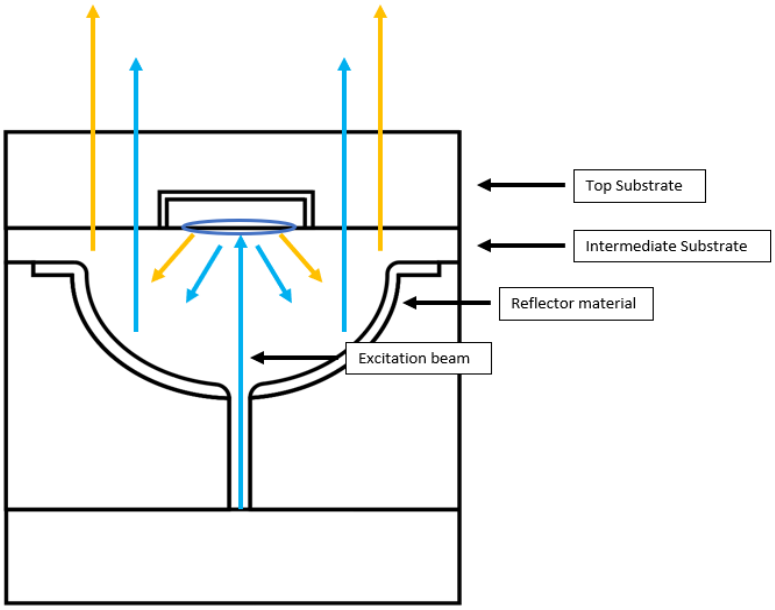

A method for manufacturing the stack:

Steps include pico-laser seed ablation of a silicate substrate, photolithography in preparation for etching the silicate substrate to generate desired the curvature of the micro-mirror (less than 100 μm diameter), coating the silicate with a reflective material (e.g., Al, Ag, Au) creating a surface reflectance (this can be lightly etched to make the surface Lambertian), creating the holes for laser light emission, reconstructing (reconstitution) the metalized silicon in a dielectric or oxide substrate making the material into a monolithic layer, stacking then bonding the reconstructed phosphor layer on top, bonding the emission layer at the bottom.

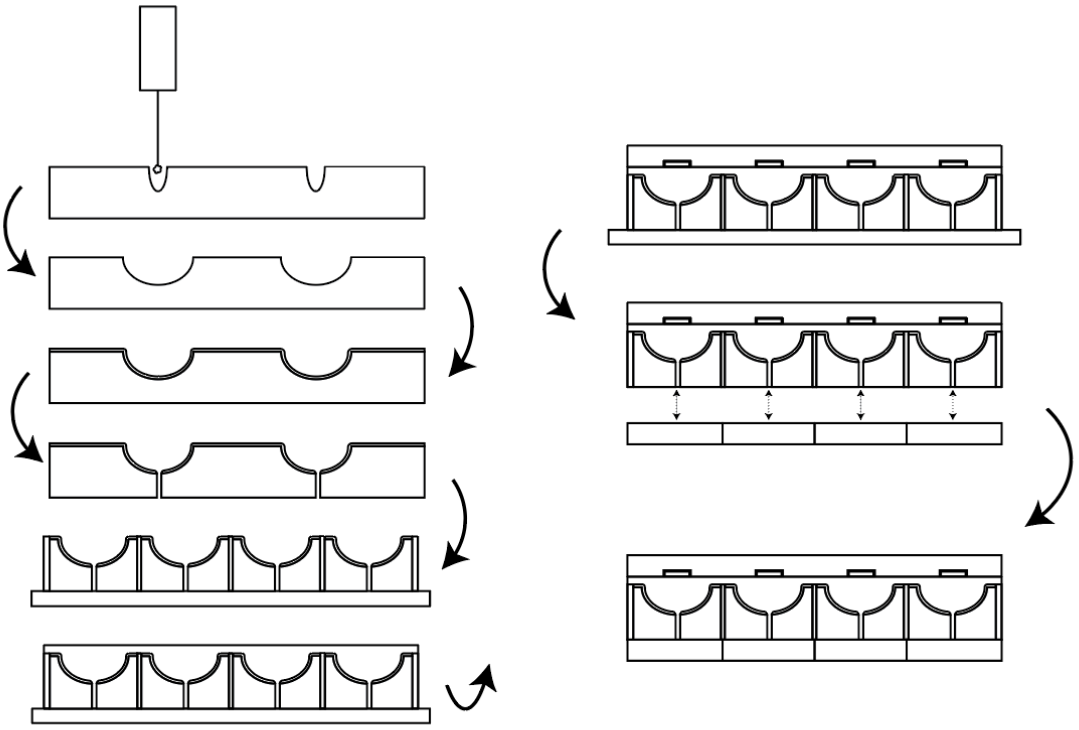

Method for creating the phosphor layer: segmenting micro-phosphor chips, metalizing the layer with a reflective coating, reconstructing the metalized phosphors into a monolithic work piece.

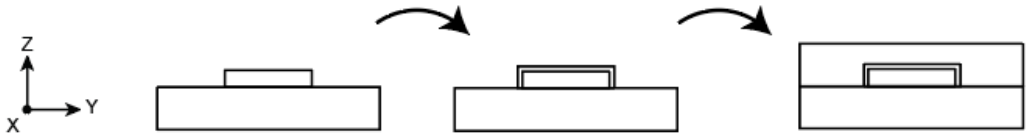

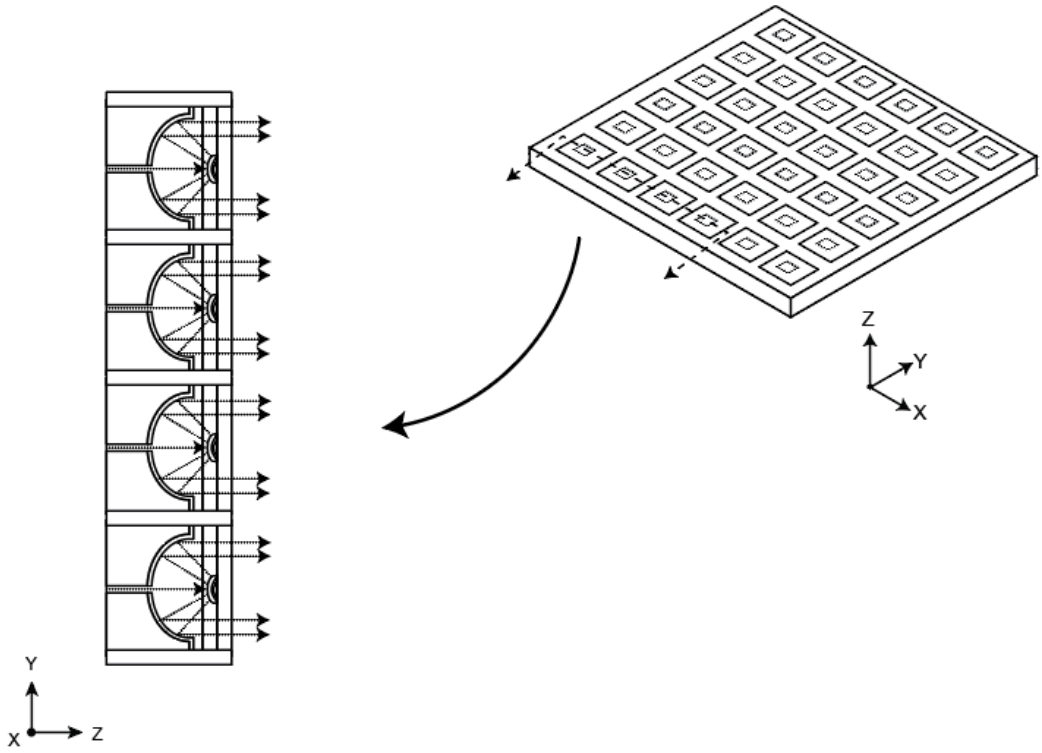

The bottom stack of the IC LtP LED may use a multitude of light sources as already discussed herein, a few examples in the drawings include VCELs, stackable ELEDs, a micro-laser or a combination thereof.

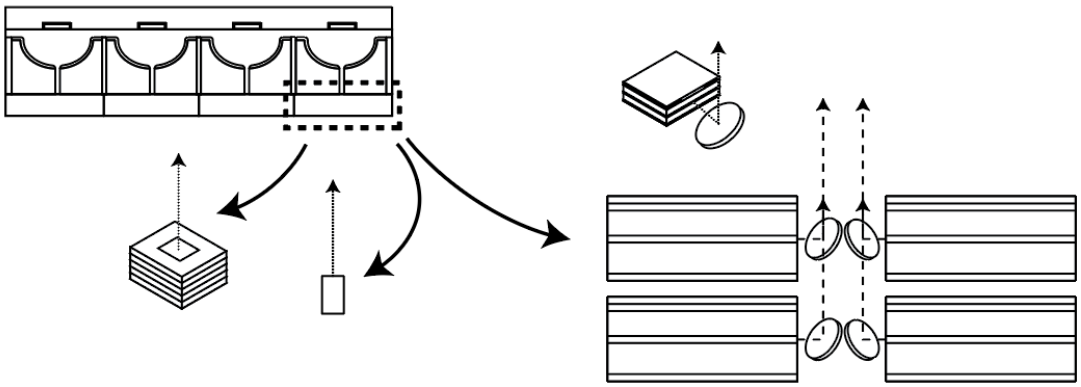

An array configuration comprising both micro and mini-LEDs:

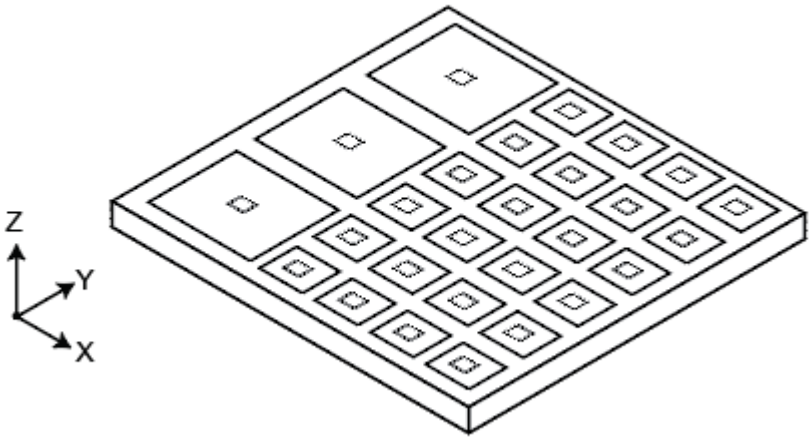

The array configuration (micro-LED display) comprising different phosphors wherein a pixel can be thought of as a combination of IC LtP pixels with different wavelengths of light to generate color for a display[23]. At the bottom, four IC LtP pixels in combination with a lens system to generate a beam. These pixels can include a phosphor layer for generating IR radiation, or a broadband phosphor excited by UV radiation.

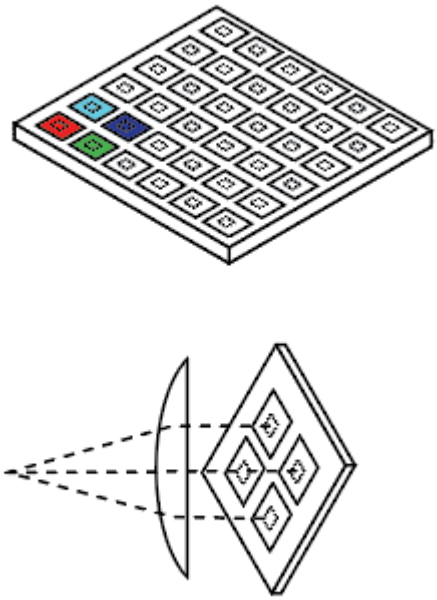

Application for this device, automotive exterior lighting, display systems requiring HiB (e.g., AR/VR), Lifi and IR sources for camera devices.

[23] Colors may include red, green, blue, cyan and or white.

Increasing the size of the pixel allows the IC LtP array for auxiliary lamps, or other exterior function lamps, a column may comprise an IR phosphor to integrate IR light projection into the lamp with vis-light patterns.

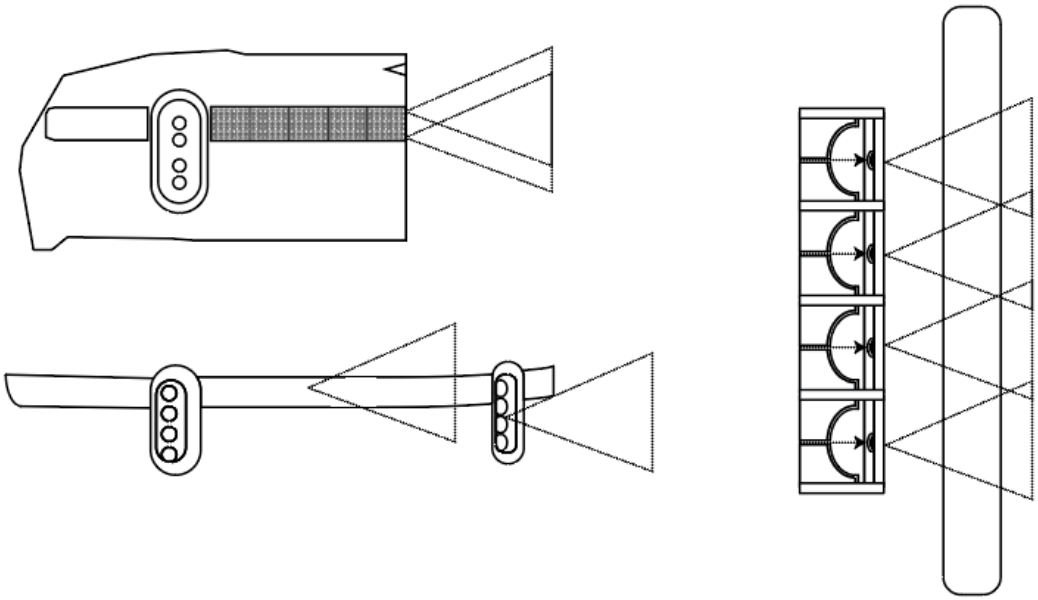

V. Appendix

The luminous efficacy simulated for the final system was observed to be 323, with the CCT having a value of 5248 K which is an off white-yellow color.

Name	Value
L/W	323
CCT	5248 K
Phosphor (t)	0.0805 mm
MPS	120 nm

Table 9. Simulation error per number of rays

1,000,000.00	Standard Deviation	18.06272	Avg	17.78866
			FLUX	**176.2112**
10,000,000.00	**Forward simulation**		Min	0.008727
	Error estimate at Peak	3.379408	Max	55.82423
	Standard Deviation	17.8613	Avg	17.85422
			FLUX	**176.366**
20,000,000.00	**Forward simulation**		Min	0.068232
	Error estimate at Peak	2.376029	Max	54.21538
	Standard Deviation	17.84403	Avg	17.84472
			FLUX	**176.378**
50,000,000.00	**Forward simulation**		Min	0.078814
	Error estimate at Peak	2.137494	Max	53.07509
	Standard Deviation	17.84495	Avg	17.84596
			FLUX	**176.3923**
70,000,000.00	**Forward simulation**		Min	0.144864
	Error estimate at Peak	1.300872	Max	51.9664
	Standard Deviation	17.84168	Avg	17.85218
			FLUX	**176.3899**
100,000,000.00	**Forward simulation**		Min	0.144864
	Error estimate at Peak	1.300872	Max	51.9664
	Standard Deviation	17.84168	Avg	17.85218
			FLUX	**176.3899**

		Spectral			Quantity
		Radiometric	**Spectral**	**Photopic (Photometric)**	
Spatial	**Flux**	Power watts (W) Φ_e	Power/wavelength interval (W/nm) Φ_λ	Luminous flux lumens (lm) = cd/sr Φ_v	*Power*
	Flux/area	Irradiance (W/m^2) E_e	Spectral irradiance (W/m^2 nm) E_λ	Illuminance (lm/m^2) or (lux)= cd sr/m^2 =lm/m^2 E_v	*Power per unit area*
	Flux/solid angle	Radiant (intensity) (W/sr) $I_{e,\Omega}$	Spectral intensity (W/sr nm) $I_{\lambda,\Omega}$	Luminous intensity candela (cd) = lm/sr $I_{v,\Omega}$	*Power Per Unit Solid Angle*
	Flux/area solid angle	Irradiance (W/m^2) L_e	Spectral radiance (W/m^2 sr nm) L_λ	Luminance lm/m^2 sr = cd/m^2 = nit L_v	*Per Unit Area Per Unit Sold Angle*

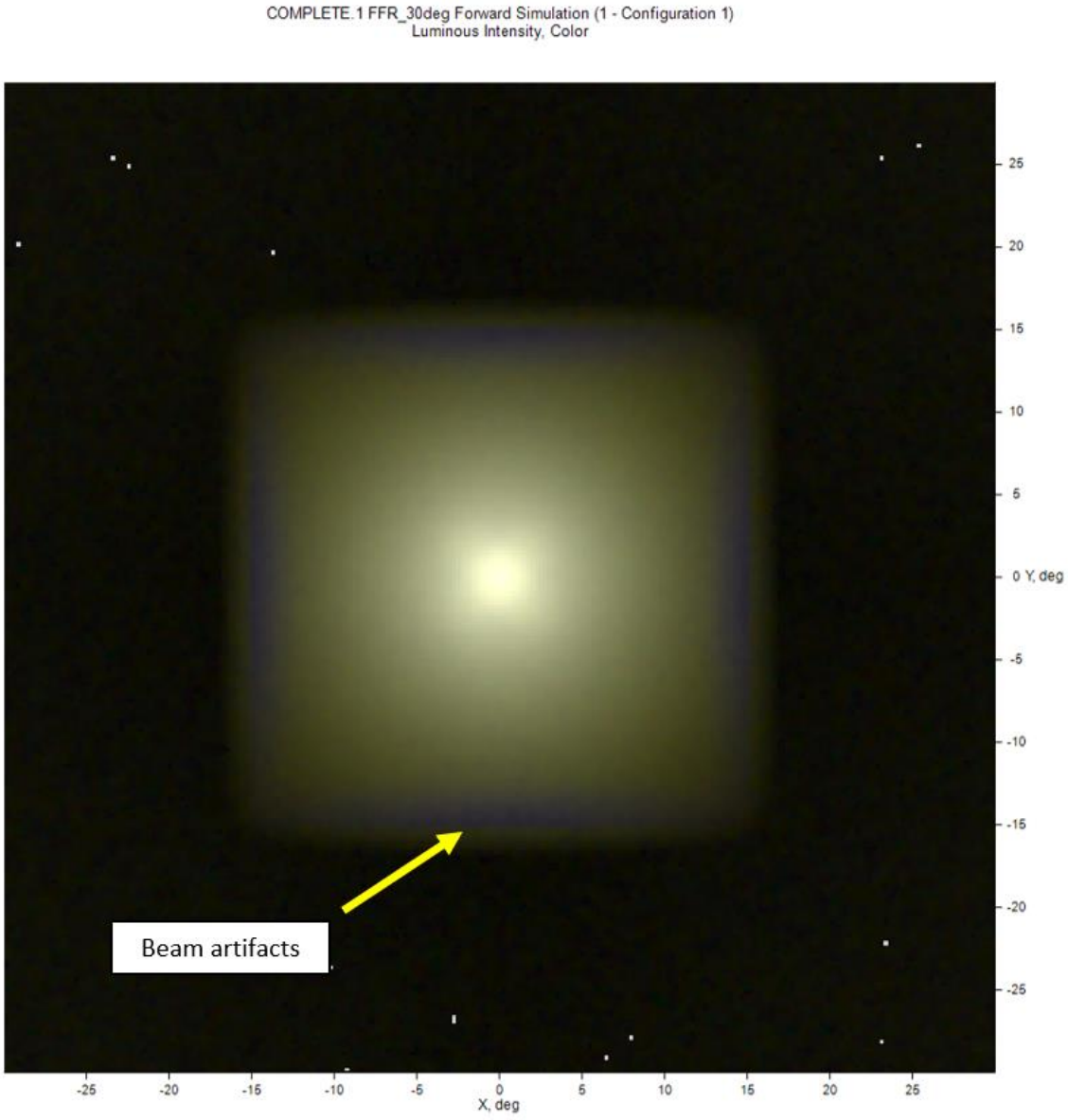

Appendix 1. Simulation results illustrating beam artifacts in the far field. The beam artifacts comprise of unconverted laser light refracted by the phosphor.

Name	Value
REFLECTOR_CURVATURE (mm)	16.39956951
PHOSPHOR_Z (mm)	0.005216797
PHOSPHOR_THICKNESS (mm)	0.001517128
PHOSPHOR_VOLUME MIE (%)	94.75010425
PHOSPHOR_PARTICLE_RADIUS (nm)	39.6177382
LASER_WAVELENGTH (nm)	450
LASER_Z (mm)	-0.06
REFLECTOR_K CONSTANT	-1
REFLECTOR_HALFWIDTH	0.045
REFLECTOR_Z	-0.046
LASER_GAUSSIAN_ANGULAR (deg)	1
LASER_GAUSSIAN_SPATIAL (mm)	0.0015
PHOSPHOR_WIDTH (mm)	0.019624301
PHOSPHOR_HEIGHT (mm)	0.018950763

Appendix 2. LT Table listed results of optimized variables.

Variables (Θ =1.5°)	Values
LUMENS 360 deg	344.9053
MAX INTENSITY 30 deg	27316.16
LUMENS 30 deg	331.7147
CIE X AVG	0.367173
CIE Y AVG	0.425064
CCT (K)	4597

(A)

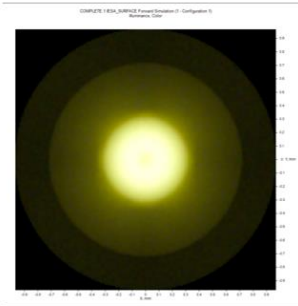

(B)

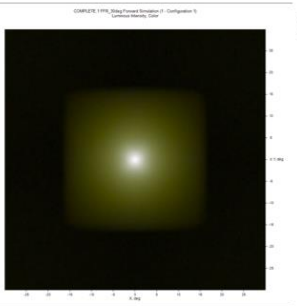

(C)

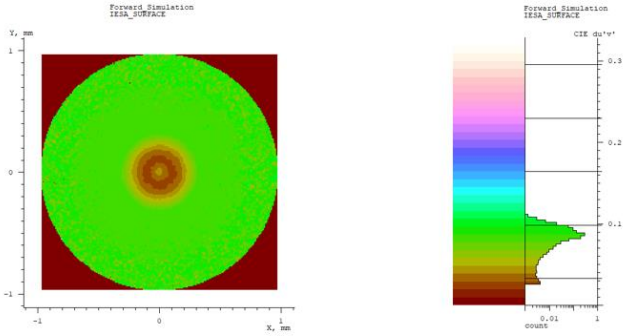

Results for 1.5 deg angular gaussian.

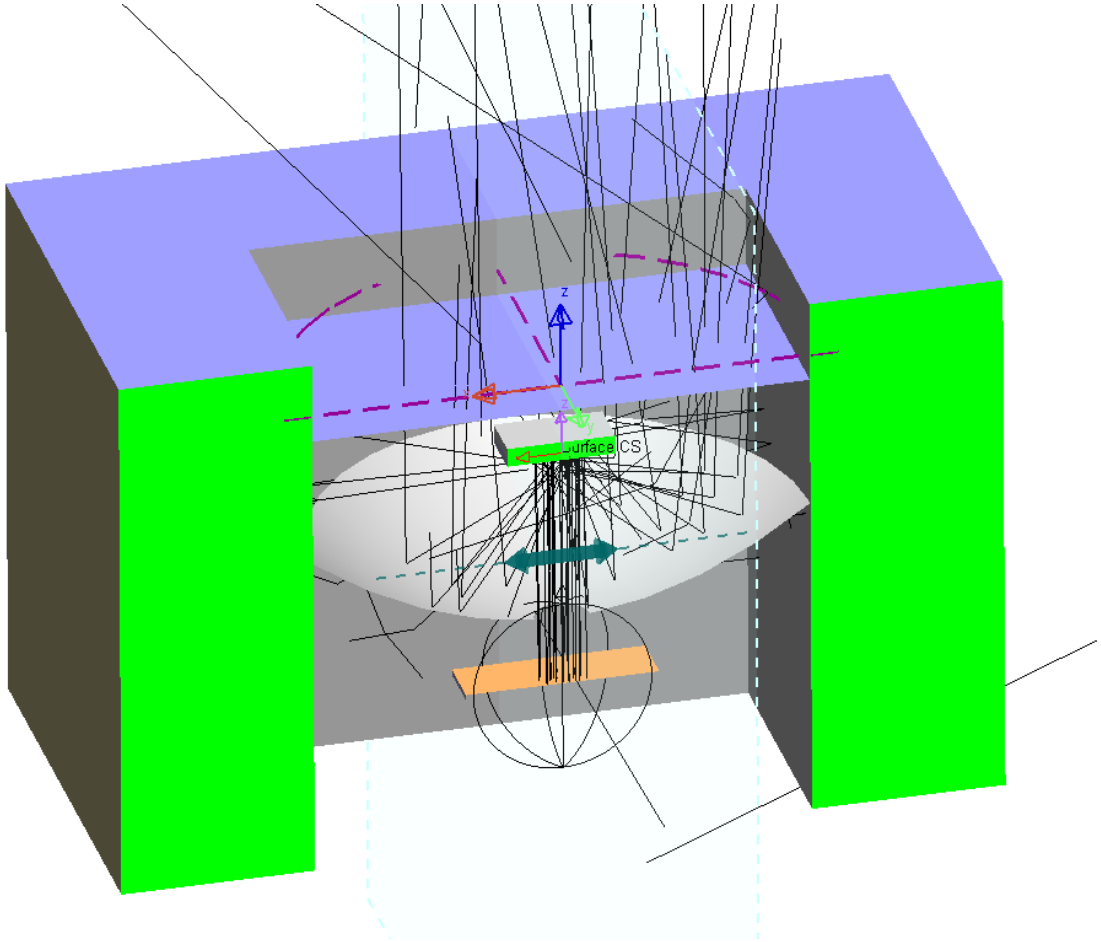

Isometric schematic of IC LtP LED with ray trace.

LucidShape Check Rayfile script

```
installation directory = C:\LucidShape_2019.09
script path: C:\LucidShape_2019.09/tasks/rayFileTools.do
 preprocessor time : 0.0 sec

load shell script: C:\LucidShape_2019.09/tasks/rayFileTools.do
ray file ""; type: LucidShape Spectral binary
ray flux = 323.502; scale factor = 1; total flux = 323.502 lm
file: C:\Users\Mykol\OneDrive - University of Arizona\COMPLETE\MICRO_WHT_1M.1.ray;
number of rays = 781274
ray file type: LucidShape Spectral binary
Bounding box of ray start points:
min,max X=-0.0999718,0.0999968
min,max Y=-0.1,0.0999968
min,max Z=-0.00471482,0.1

min,max I=5.07979e-06,0.999928
0 null rays I <= 1.19209e-07
263915 rays I in [0%,10%] range
22557 rays I in [10%,20%] range
25922 rays I in [20%,30%] range
30434 rays I in [30%,40%] range
32334 rays I in [40%,50%] range
38342 rays I in [50%,60%] range
37369 rays I in [60%,70%] range
56823 rays I in [70%,80%] range
72093 rays I in [80%,90%] range
201485 rays I in [90%,100%] range
total 781274 checked rays
```

VI. References

[1] Angelo V. Arecchi, T. M. (2014). *Field Guide to Illumination.* Bellingham: SPIE .

[2] Anne C. Berends, M. A. (2020). YAG:Ce3+ Phosphor: From Micron-Sized Workhorse for General Lighting to a Bright Future on the Nanoscale. *Chemical Reviews*, 13461-13479.

[3] Barry, K. (2022). *Smart Adaptive Headlights Will Soon Brighten U.S. Roads.* https://www.consumerreports.org/cars/car-safety/smart-adaptive-headlights-will-soon-brighten-us-roads-a8128257819/: Consumer Reports.

[4] Bass, M. (2010). Handbook of Optics, Third Edition Volume II. In R. J. Koshel, *Lighting and Application* (p. 40.1). McGraw Hill.

[5] Cao, Y., Chen, W., Du, Y., Gaojin Qi, T. S., Zhang, G., & Fan, J. (2022). Luminous Performances Characterization of YAG: Ce3+ Phosphor/Silicone Composites Using Both Reflective and Transmissive Laser Excitations. *IEEE*, https://ieeexplore.ieee.org/document/9712174.

[6] CRYTUR. (2024, 02 01). *YAG:Ce*. Retrieved from CRYTUR USA: https://www.crytur-usa.com/materials/yagce/

[7] Dong-Ho Lee, J.-Y. J.-K. (2015). Modeling of reflection-type laser-driven white lighting considering phosphor particles and surface topography. *Optical Society of America* , https://opg.optica.org/directpdfaccess/bae2716e-0a5e-4667-8ce47ef8387f8bd3_322633/oe-23-15-18872.pdf?da=1&id=322633&seq=0&mobile=no.

[8] DOW. (2024, 02 1). *SILASTIC™ MS-1001 Moldable Silicone*. Retrieved from DOW: https://www.dow.com/en-us/pdp.silastic-ms-1001-moldable-silicone.04117871z.html#tech-content

[9] Eiji Miyai, K. S. (2008). Linearly-Polarized Single-Lobed Beam in a Surface-Emitting Photonic-Crystal Laser. *Applied Physics Express*, https://iopscience.iop.org/article/10.1143/APEX.1.062002/pdf.

[10] EP&T. (2024). *EPI Wafer Reconstitution Process*. Retrieved from Electronic Products & Technology: Canada: https://www.ept.ca/features/ar-display-systems-are-the-new-reality/epi-wafer-reconstitution-process/

[11] Field Guide to Atmospheric Optics, S. E. (2019). *Larry C. Andrews.* ISBN 9781510619371: SPIE.

[12] Hahn, D. W. (2009). *Light Scattering Theory* . Department of Mechanical and Aerospace Engineering, University of Florida.

[13] James W. RARING, P. R. (2018). *USA Patent No. US10879673B2.*

[14] JUSTIN C.JOHNSON, K. P. (2002). Single gallium nitride nanowire lasers. *Nanowires Letters UC Berkeley*, https://nanowires.berkeley.edu/wp-content/uploads/2013/01/060.pdf.

[15] Kaplan, A. (2023, May 11). *Blinded by the light: Cars in the U.S. still lack glare-reducing headlights*. Retrieved from NBC News: https://www.nbcnews.com/news/us-news/blinded-light-american-headlight-safety-lags-years-countries-rcna82666

[16] Kei Emoto, T. K. (2022). Wide-bandgap GaN-based watt-class photonic-crystal lasers. *Nature: Communications Materials*, 72.

[17] Koshel, R. J. (2013). *Illumination Engineering: Design with Nonimaging Optics.* Hoboken: WILEY.
[18] Kouno, T. S. (2016). Crystal structure and optical properties of a high-density InGaN nanoumbrella array as a white light source without phosphors. *NPG Asia Materials*, 8.
[19] Kumler, J. (2001). Designing and Specifying Aspheres for Manufacturability. *Current Developments in Lens Design and Optical Engineering*.
[20] Lee, T.-Y. (2023). Optimized Design with Artificial Intelligence Quantum Dot White Mini LED Backlight Module Development. *Semiconductor Nanocrystal Studies for Optoelectronic Applications*, https://www.mdpi.com/2073-4352/13/10/1411.
[21] LightTools®. (2024). *Illumination Module User's Guide.* Retrieved from Synopsys® LightTools®.
[22] Linhart, O. Z. (2022). Engineering of YAG:Ce to improve its scintillation properties. *Optical Materials*, 100165.
[23] Mertens, R. (2024). *The MicroLED Handbook.* https://www.microled-info.com/microled-handbook.
[24] Mu Ku Chen, Y. W. (2021). Principles, Functions, and Applications of Optical Meta-Lens. *Advanced Optical Materials*, https://onlinelibrary.wiley.com/doi/full/10.1002/adom.202001414.
[25] NHTSA. (2022, February 15). *NHTSA to Allow Adaptive Driving Beam Headlights on New Vehicles, Improving Safety for Drivers, Pedestrians, and Cyclists*. Retrieved from NHTSA: https://www.nhtsa.gov/press-releases/nhtsa-allow-adaptive-driving-beam-headlights-new-vehicles-improving-safety-drivers
[26] OSRAM. (2024, 02 02). *µAFS LED headlights*. Retrieved from OSRAM Automotive: https://www.osram.co.uk/am/specials/trends-in-automotive-lighting/%C2%B5afs-led-headlights/index.jsp
[27] Overton, G. (2017, February 22). *Laser Lighting: White-light lasers challenge LEDs in directional lighting applications*. Retrieved from Laser Focus World: https://www.laserfocusworld.com/lasers-sources/article/16548296/laser-lighting-white-light-lasers-challenge-leds-in-directional-lighting-applications
[28] *Rayleigh Scattering, Mie Scattering.* (2015). Retrieved from Perdue University: https://engineering.purdue.edu/wcchew/ece604f19/Lecture%20Notes/Lect34.pdf
[29] Robertson, A. (1968). Computation of Correlated Color Temperature and Distribution Temperature. *JOSA*, 1528.
[30] Rosin, S. (1968). Inverse Cassegrainian Systems. *OPTICA*, 1483-1497.
[31] Shuxing Li, Y. G.-J. (2022). Laser Phosphors for Next-Generation Lighting Applications. *Accounts of Material Research*, https://pubs.acs.org/doi/full/10.1021/accountsmr.2c00193?ref=recommended.
[32] Shuxing Li, Y. X. (2019). Data-driven Discovery of Full Visible-Spectrum Phosphors. *Chemistry of Materials*, 6286-6294.
[33] Shuyang Bao, Y. L. (2022). Superhigh-Luminance Ce:YAG Phosphor in Glass and Phosphor-in-Glass Film for Laser Lighting. *ACS Sustainable Chemistry & Engineering*.

[34] STANLEY LTD. (2024, 02 02). *LCD-ADB Systems*. Retrieved from STANLEY : https://www.stanley.co.jp/e/technology/innovation/lcd-adb.html

[35] Taoli, D. (2022). Achieving High Light Uniformity Laser-driven White Lighting Source by Introducing Secondary Phases in Phosphor Converters. *Journal of Inorganic Materials*, 891-896; https://www.jim.org.cn/EN/10.15541/jim20220074.

[36] Tomotaka Asari, M. M. (2021). Adaptive driving beam system with MEMS optical scanner for reconfigurable vehicle headlight. *Journal of Optical Microsystems*, 014501; https://www.spiedigitallibrary.org/journals/journal-of-optical-microsystems/volume-1/issue-01/014501/Adaptive-driving-beam-system-with-MEMS-optical-scanner-for-reconfigurable/10.1117/1.JOM.1.1.014501.full?SSO=1#_=_.

[37] Ulrich, L. (2013). Whiter brights with lasers. *Spectrum IEEE*, 35-65.

[38] Wang, T., Silva, J. L., Daily, R., Capuz, G., Gonzalez, M., Rebibis, K. J., . . . Beyne, E. (2013). Wafer reconstruction: An alternative 3D integration process flow. *IEEE*, https://ieeexplore.ieee.org/document/6745754#citations.

[39] Yiman Wang, H. Z. (2014). Modeling on phosphor sedimentation phenomenon during curing process of high power LED packaging. *Journal of Solid State Lighting*.

[40] Yiman Wang, H. Z. (2014). Modeling on Phosphor Sedimentation Phenomenon During Curing Process of High Power LED Packaging. *Journal of Solid State Lighting*, https://journalofsolidstatelighting.springeropen.com/counter/pdf/10.1186/2196-1107-1-2.pdf.

[41] Yirong Xu, S. L. (2019). A search for extra-high brightness laser-driven color converters by investigating thermally-induced luminance saturation. *Journal of Materials Chemistry C* , https://pubs.rsc.org/en/content/articlelanding/2019/tc/c9tc03919h#fn1.

[42] Yuanbin Gao, C. C.-H. (2023). Influence of anti-phase surface relief structure on optical mode and laser output power for 450 nm GaN-based VCSELs. *Japanese Journal of Applied Physics*, 62.

[43] Zollers, M. (2011). *Phosphor Modeling in LightTools® Ensuring Accurate White LED Models* . https://www.Synopsys®.com/content/dam/Synopsys®/optical-solutions/documents/datasheets/modeling-phosphors-in-lighttools.pdf: Synopsys®.